INTERNATIONAL SCHOOL FOR ADVANCED STUDIES
Theory and Numerical Simulation of Condensed Matter

Quantum mechanical modeling of nano magnetism

New tools based on density-functional-theory with case applications to solids, surfaces, wires, and molecules

Thesis submitted for the degree of
Doctor Philosophiæ

Candidate
Adriano Mosca Conte

Supervisors
Dr. Stefano Fabris
Prof. Stefano Baroni

February 2007

Contents

Introduction

Molecular nanomagnets are gaining more and more importance in science and technology for their electronic, chemical, and also biomedical applications. The origin of this interest is in their behavior as single domain magnets. This is due to their tiny dimensions that can range from few nanometers to hundreds or also thousands of nanometers. In the case of electronic applications for instance, one of the main challenges is to reduce the size of magnetic storage media, while preventing the single memory units to interact with each other. The most promising materials for this purpose are single domain magnetic nanoparticles and molecular nanomagnets. Magnetic nanoparticles supported by metallic surfaces are the subject of several experimental studies [1, 2]. These structures also find application in catalysis and could be employed as electronic receptors, as magnetic storage media [3], or for quantum computing [4].

While for most of the bulk systems the magnetic phenomena are well understood, the mechanisms that control the magnetism in nanomagnets are not yet clear with the same level of details. The goal of this thesis is to use density functional theory (DFT) to investigate the structural, electronic, and magnetic properties of low-dimensional systems and nanostructures, focusing on the effects of magnetic anisotropy that are known to be crucial for stabilizing magnetism in these systems.

Macroscopic ferromagnetic or ferrimagnetic materials are characterized by the formation of magnetic domains separated by walls (see Fig. 1). The number of domains in a solid and their thickness result from the balance between the external magnetostatic energy and the energy due to the presence of the walls: the former tends to rise the number of domains, the latter to reduce it.

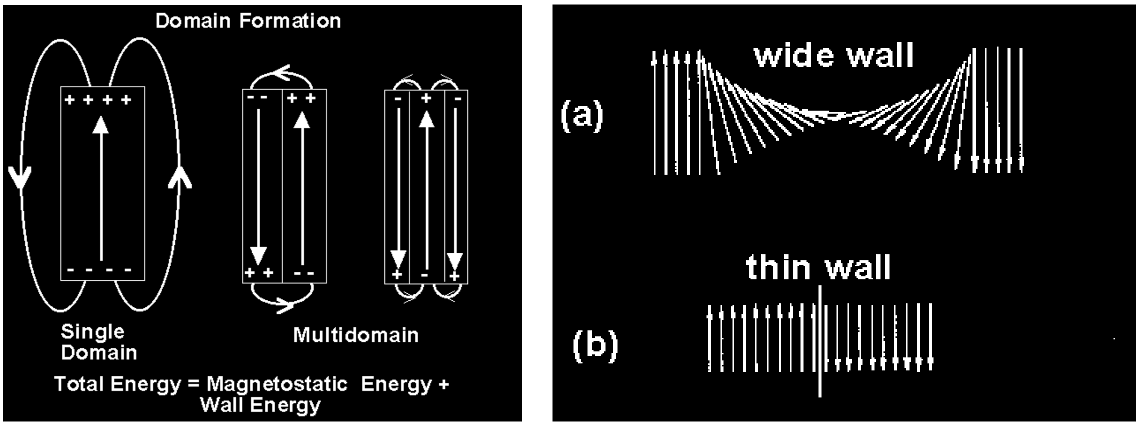

Figure 1: Magnetic domains

Below the Curie temperature and in the absence of external magnetic fields, the total magnetization of a macroscopic magnet ranges from zero to a maximum value, called remanence; above this temperature the material becomes paramagnetic.

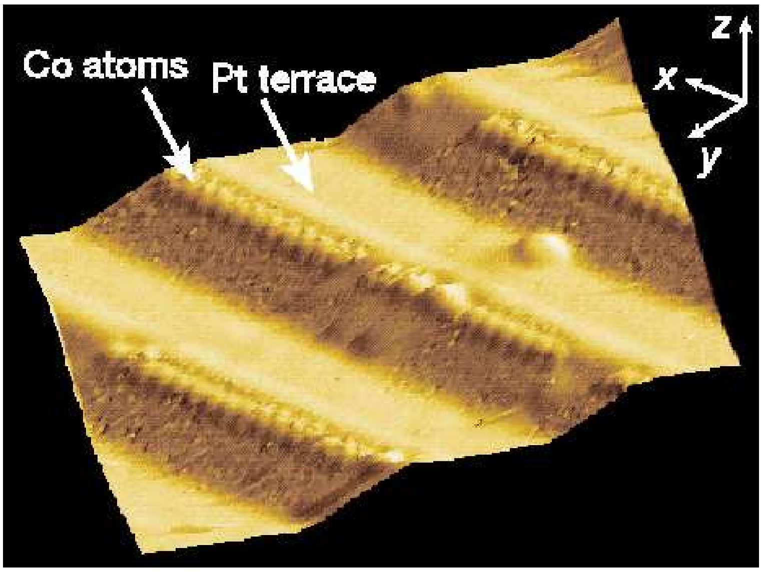

Figure 2: Co nanowire on a (997) Pt surface.

According to a theorem by Mermin and Wagner [5, 6], no finite temper-

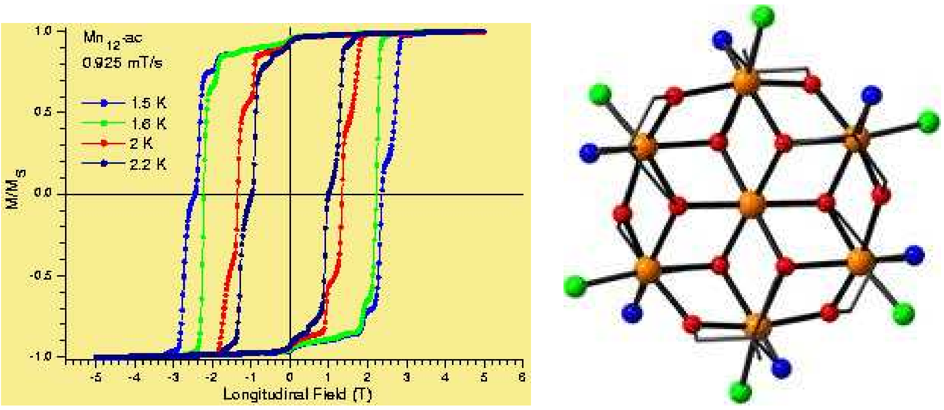

Figure 3: Hysteresis loop of the Mn_{12}-complex.

ature transition can break a continuous symmetry in dimensions lower than 3. As a consequence nanowires (D = 1) and single domain particles (D = 0) cannot form stable magnetic ordered structures at any finite temperature. However, under the so called blocking temperature, these systems may be able to maintain a ferromagnetic order for a period that can be much longer than the typical time for an experimental observation or for the functional activity of a device. Magnetism in low dimensional systems is a kinetic effect due to the stabilizing action of the magnetic anisotropy resulting from the spin-orbit interaction. It is this phenomenon that allows the formation of magnetic 1D systems, like the one reported in Fig. 2, consisting of a Co nanowire supported by a (997)-Pt surface [7]. At a temperature of a few Kelvins this wire forms stable series of atoms (15 on average) with magnetic moments parallel to each other. An example of a 0D magnetic system is the Mn_{12}-complex [8] reported in Fig. 3. This nanomagnet presents an easy magnetization axis below a blocking temperature of 3 K [9]. In the same figure it is possible to see its measured hysteresis loop denoting its ferromagnetic character.

The ferromagnetic behavior of some low dimensional systems can be traced back to the magnetic anisotropy of materials, which is ultimately due to the relativistic spin-orbit effect. By decreasing the dimension of a system under the typical size of a magnetic domain, the material becomes single domain. As its size continues to decrease within the single domain range, another critical threshold can be reached, at which remanence goes to zero. When this happens, the system becomes superparamagnetic. At low temperature, a single domain particle of volume V has a uniform magnetization. The energy of the system reaches its minimum when the magnetization lays along a specific direction called easy magnetization axis; the energy is maximal when the magnetization lays parallel to the so called hard magnetization direction. The difference between these two energies is the magnetic anisotropy energy (MAE). If V is small enough, or the temperature is high enough, the thermal energy ($K_B T$) is sufficient to overcome the anisotropy energy, and a single domain particle behaves like a superparamagnet. For superparamagnetic particles, the net magnetic moment in zero field and at finite temperature, averages to zero. In an applied field, there is a net statistical alignment of magnetic moments. This is analogous to paramagnetism, except now the magnetic moment is not that of a single atom, but of a single domain particle containing many atoms. Hence, superparamagnets display a much higher susceptibility than that of simple paramagnets. In response to a change in applied field or temperature, an ensemble of superparamagnetic particles will approach an equilibrium value of magnetization with a characteristic relaxation time according to the Arrhenius formula which regulates the thermal activation processes. In the specific case, this formula takes the form first derived by Néel [10]:

$$\frac{1}{\tau} = f_0 \exp\left[\frac{-K_u V}{k_B T}\right]. \tag{1}$$

Here, f_0 is the frequency factor (measured in sec^{-1}); K_u is the anisotropy constant and depends, at the microscopic scale, mostly on the spin-orbit interaction; V is the particle volume and is proportional to the magnetic moment of the particle; k_B is the Boltzmann constant, and T is the absolute temperature. The exponential nature of the relaxation time on V and T makes it possible to define a blocking temperature, T_B (at constant volume), or blocking volume V_B, (at constant temperature) at which the magnetization goes from an unstable condition ($\tau \ll t$) to a stable condition ($\tau \gg t$); t in this case indicates the experimental observation time. A difference in temperature of few degrees can correspond to a change in relaxation time of the order of 10^{16} sec. Therefore the blocking temperature in single-domain materials is analogous to the Curie temperature in macroscopic magnetic systems. The concept of blocking temperature is extended to all magnetic systems with a dimensionality smaller than two, as for example nanowires, and in general to all the nanomagnets, which are in principle prevented to be ferromagnetic but have a large relaxation time at low temperature.

The electronic structure of magnetic systems is most commonly studied using DFT within the local spin density approximation (LSDA). In the LSDA each molecular orbital is assumed to be fully spin-polarized. This approximation is sufficient for the majority of the structures, but it is not adequate to study nanomagnets because of two limitations: i) the assumption of a fixed magnetic polarization axis prevents the study of noncollinear magnetic configurations, and ii) most of the standard calculations neglect the spin-orbit term, which is essential to capture the magnetic anisotropy of nanomagnets. Traditionally, many DFT studies of magnetism are performed by all-electron calculations, often in conjunction with some shape approximation on the potential, like for example the Korringa-Kohn-Rostoker (KKR) method [11, 12] or the linear muffin-tin orbital with atomic-spheres approximation (LMTO-ASA) [13]. These methods, however, are inaccurate and/or inefficient in the calculation of the equilibrium atomic geometries on which magnetic properties depend very sensitively.

Plane-wave pseudo-potential methods are much more efficient than all-electron ones to calculate the atomic forces and hence to determine the equilibrium geometries. Modern pseudo-potential methods based on so called ultrasoft pseudo-potential [14] are traditionally limited to non-relativistic calculations that cannot capture magnetic anisotropy effects. The purpose of this thesis is to develop a computational framework able to combine the efficiency and accuracy of modern ultrasoft pseudopotentials with a fully relativistic treatment of the electron spin, which is ultimately responsible for the magnetic anisotropy effects that stabilize the magnetic structure of nanomagnets.

The thesis is organized as follows. The basis of density functional theory and its extension to magnetic systems is reviewed in the first chapter. The second chapter describes the implementation of the fully relativistic ultrasoft pseudopotential method whose predictive power is tested by calculating the spin-orbit splittings in the band structure of two bulk systems: Au-fcc and Pt-fcc. In the third chapter the magnetic properties of several Co based nanostructures are described as a function of their dimensionality, going from 2D to 0D systems. Finally, in the fourth chapter, the physical properties of a novel class of molecular nanomagnets are discussed. Mathematical developments and details of some of the topics mentioned during the thesis are reported separately as appendices.

Chapter 1

Density functional theory of magnetism

This chapter provides a short overview of the concepts that are used to describe magnetism within DFT, including the generalizations necessary to study noncollinear magnetic systems. As an example I present an application to Fe$_5$ clusters.

1.1 Density Functional Theory

In 1964 Hohenberg and Kohn published a ground-breaking article [15], which lead to the development of what is known today as *density functional theory* (DFT). They considered a system of interacting electrons in an external potential, $V(\mathbf{r})$. While it is clear that $V(\mathbf{r})$ determines, via the Schrödinger equation, the ground state energy of the system, Hohenberg and Kohn showed that there exists a functional F[n] such that the ground state energy can be expressed as the minimum of the functional

$$E_V[n] = F[n] + \int d\mathbf{r}\, V(\mathbf{r})n(\mathbf{r}), \tag{1.1}$$

where $n(\mathbf{r})$ is the charge-density, and $F[n]$ does not depend on the system. This fact makes it possible to describe, at least in principle, the ground state properties of a system of interacting electrons in terms of the charge-density only, rather than on the far more complicated many-particle wavefunction.

One year later, Kohn and Sham [16] proposed a practical scheme to perform such calculations. To this end, they introduced an auxiliary system of non-interacting electrons for which the ground state charge-density distribution can be expressed in terms of one-electron orbitals as:

$$n(\mathbf{r}) = \sum_i^{occ.} \psi_i^*(\mathbf{r})\psi_i(\mathbf{r}), \tag{1.2}$$

where the sum is over all the occupied states. In terms of the ψ_i's the ground state energy can be expressed as minimum of the auxiliary functional:

$$\begin{aligned} E[\psi,\psi^*,V] =& T[\psi,\psi^*] + E_H[n(\psi,\psi^*)] + E_{xc}[n(\psi,\psi^*)] + \\ & \int d\mathbf{r}\, V(\mathbf{r}) n(\psi(\mathbf{r}),\psi^*(\mathbf{r})), \end{aligned} \tag{1.3}$$

where

$$T[\psi,\psi^*] = -\frac{\hbar^2}{2m}\sum_i^{occ.}\int d\mathbf{r}\, \psi_i^*(\mathbf{r})\nabla^2\psi_i(\mathbf{r}), \tag{1.4}$$

E_H is the Hartree energy (essentially the classical Coulomb interaction of the ground state charge density distribution), and E_{xc} is the so called exchange-correlation energy. Variation of this functional with respect to ψ_i^* leads to the so called Kohn-Sham (KS) equation:

$$\left(-\frac{\hbar^2}{2m}\nabla^2 + V_{ext}(\mathbf{r}) + V_H(\mathbf{r}) + V_{xc}(\mathbf{r})\right)\psi_i(\mathbf{r}) = \varepsilon_i\psi_i(\mathbf{r}), \tag{1.5}$$

where

$$V_H(\mathbf{r}) = \frac{\delta E_H}{\delta n(\mathbf{r})} = e^2\int d\mathbf{r}'\, \frac{n(\mathbf{r}')}{|\mathbf{r}-\mathbf{r}'|}, \tag{1.6}$$

and

$$V_{xc}(\mathbf{r}) = \frac{\delta E_{xc}}{\delta n(\mathbf{r})}. \tag{1.7}$$

While this pioneering work made DFT-based calculations feasible in principle, one important problem remained: the development of good approximations for the exchange-correlation energy-functional. The most commonly used form of this functional is the so-called local density approximation (LDA) which consists in deriving the exchange-correlation functional from the properties of an homogeneous electron gas. In this approximation, one writes

$$E_{xc} = \int d\mathbf{r}\, n(\mathbf{r}) \varepsilon_{xc}(n(\mathbf{r})), \tag{1.8}$$

where $\varepsilon_{xc}(n)$ is the exchange-correlation energy per particle of a homogeneous electron gas with density $n(\mathbf{r})$. This quantity has been calculated accurately using quantum Monte-Carlo techniques [17]. A considerable effort has been put into the development of more precise approximations for this functional (some important examples are reported in Refs. [18, 19]), and today this is still a very active and challenging field of research.

1.2 The plane-wave pseudopotential method

The KS equation, Eq. (1.5), can be solved in practice by expanding the KS orbitals in a finite set of basis functions. Among the various existing options, we limit our discussion to the plane wave (PW) basis set: besides their conceptual simplicity, PW's have invaluable numerical advantages. Compared to other basis sets, the PW's allow to express the physical forces acting on the ions as the Hellman-Feynman forces, without adding auxiliary terms. Moreover the size of the basis can be increased, and checked in a systematic, and unbiased way valid for all the systems, by simply increasing the maximum kinetic energy (energy cutoff). Finally PW's allow for a simple calculation of the matrix elements of the Hamiltonian.

Unfortunately PW's cannot be straightforwardly used with Eq. (1.5) because of the fast oscillations of the core orbitals in the neighborhood of the nuclei, requiring a large basis size to be described accurately. However, core electrons are so tightly bound to the nuclei that their energy does not change when chemical bounds are formed, so that they can be effectively considered as passive spectators of chemical processes. The pseudopotential method allows to simplify the Kohn-Sham equation by eliminating all the degrees of freedom associated with the core electrons. This is done by mapping the all-electron frozen-core problem onto an equivalent problem involving valence electrons only. Formally, in the Hamiltonian, the nuclear potential is replaced by a new pseudopotential in such a way that the lowest one-electron energies coincide with the valence ones obtained by an all-electron calculation. The pseudopotential is split in a local radial potential, plus a non local contribution that depends on the angular momentum of the wavefunction to which it is applied. If the non local contribution is non local only in the angular part, the pseudopotential is said to be in a semi-local form, otherwise it is in fully separable form. Calculations based on pseudopotentials have an accuracy comparable with the all-electron calculations. The eigenfunctions obtained by solving the KS equation with the pseudopotential method are called pseudowavefunctions. In regions far enough from the nuclei of the atoms, the corresponding pseudopotentials coincide with the nuclear all-electron potentials. To be more precise, for each atom involved in the calculation, a spherical core region of radius r_c and centered on the nucleus of the atom is defined such that, outside this region, the pseudopotential is equal to the all-electron potential. Therefore, the pseudowavefunctions are proportional to the wavefunctions obtained with an all-electron calculation outside the core region, while inside they have a smooth shape compared to the all-electron wavefunctions. To guarantee a good transferability of the pseudopotentials, a stronger condition than the proportionality is required: the pseudowavefunctions must coincide with the all-electron wavefunctions outside the core region. As a consequence, the pseudowavefunctions are orthonormal only if the integral of their charge distribution inside the core region is equal to the one obtained with an all-electron calculation. Pseudopotentials that undergo to this constraint are called norm-conserving pseudopotentials. Further details on pseudopotentials can be found in Refs. [20, 21].

1.2.1 Ultrasoft pseudopotentials

In norm conserving pseudopotentials, the size of the PW's basis set required to properly describe the $2p$, $3d$, and $4f$-orbitals is very large. The example of the $2p$ orbitals of the isolated oxygen atom is reported in Fig. 1.1. The only way to generate a smooth pseudowavefunction that coincides with the all-electron wavefunction outside the core region, is to violate the condition requiring the conservation of the norm inside this region. This is not possible for norm-conserving pseudopotentials, therefore the calculations for

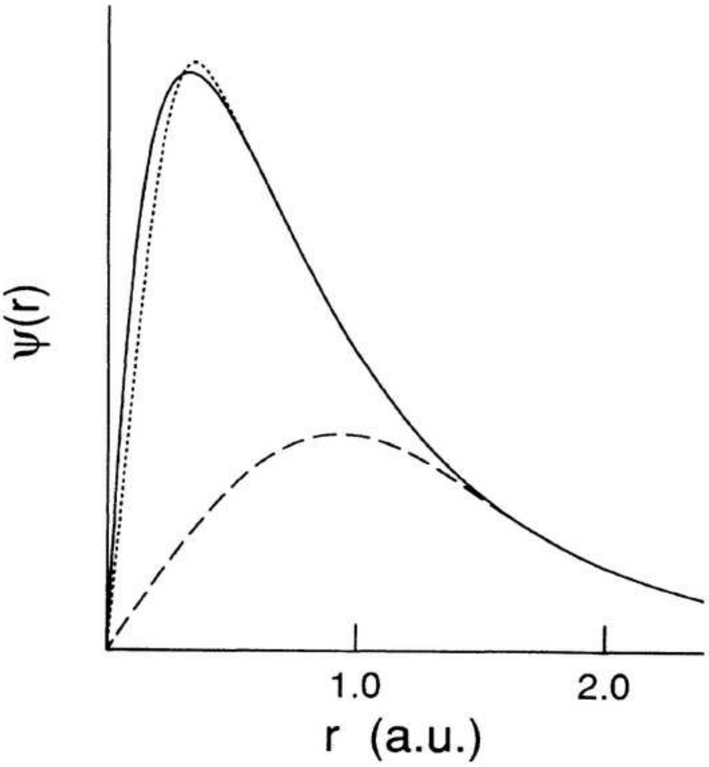

Figure 1.1: Oxygen $2p$ radial all-electron wave function (solid line), corresponding pseudowavefunctions for a norm-conserving pseudopotential (dotted line), and an ultrasoft pseudopotential (dashed line).

transition metal and rare earth atoms systems are computationally very demanding. In 1990 David Vanderbilt [14] found a method to overcome this constraint. This is possible by generalizing the eigen-problem; an operator Ŝ is defined such that the pseudowavefunctions $|\phi_{nk}\rangle$ obey the following orthonormalization law:

$$\langle\phi_{nk}|\hat{S}|\phi_{n'k}\rangle = \delta_{nn'} \tag{1.9}$$

In this way, the pseudowavefunctions are not orthonormalized and the integral of the charge-density distribution of each single pseudowavefunction inside the core region is different from the one obtained with an all-electron calculation. Their shape can be chosen to be smoother than the one of the norm-conserving pseudowavefunctions, as shown in the Figure 1.1.

The Hamiltonian problem is reformulated throughout the introduction of the operator $\hat{S}$:

$$\hat{H}|\phi_{nk}\rangle = \varepsilon_{nk}\hat{S}|\phi_{nk}\rangle \tag{1.10}$$

The usual definition of the charge density cannot simply be applyed to the ultrasoft pseudowavefunctions, since the total charge would not be conserved. To correctly reproduce the Hartree and the exchange-correlation interactions the valence charge-density is redefined in such a way to make up this charge deficit. The mathematical details of this method can be found in Ref. [14]. Pseudopotentials obtained using this method are called ultrasoft.

1.3 Extension to spin-polarized systems

In principle, the original Hohenberg-Kohn theorem also applies to systems where the polarization of the electronic spins leads to a magnetization density $\mathbf{m}(\mathbf{r})$, since the magnetization is a functional $\mathbf{m}[n]$ of the ground state charge-density, as well as any other ground state property. However the application of DFT to the spin-polarized case using the charge-density as the only functional variable would require a highly nonlocal functional for the exchange-correlation energy [22]. In practice, one resorts to a different formulation of DFT, which is also valid in the presence of an external magnetic field $\mathbf{B}_{ext}$ [23]. In this case, the energy of the system is a functional of the ground state charge-density matrix, which can be expressed in terms of the charge-density, $n(\mathbf{r})$, and of the spin magnetization, $\mathbf{m}(\mathbf{r})$. The advantage of focusing on $n(\mathbf{r})$ and $\mathbf{m}(\mathbf{r})$ rather than on the charge-density alone is that a straightforward generalization of the local density approximation is possible in this case.

A very common formulation for the exchange-correlation functional is the local spin density approximation (LSDA). In this approximation the magnetization is aligned along one fixed direction, conventionally labeled as the z axis. Therefore the x and y components of the magnetization are set to zero and the exchange and correlation density energy can be expressed as a function of the variables $n(\mathbf{r})$ and $m_z(\mathbf{r})$:

$$n(\mathbf{r}) = n_\uparrow(\mathbf{r}) + n_\downarrow(\mathbf{r}), \tag{1.11}$$

and

$$m_z(\mathbf{r}) = n_\uparrow(\mathbf{r}) - n_\downarrow(\mathbf{r}), \tag{1.12}$$

where:

$$n_\alpha(\mathbf{r}) = \sum_i^{occ} \psi_{i\alpha}^*(\mathbf{r})\psi_{i\alpha}(\mathbf{r}), \tag{1.13}$$

and $\alpha = \uparrow, \downarrow$. In this approach, one interpolates the energy density $\varepsilon_{xc}(n)$ in Eq. (1.8) between $\varepsilon_{xc}^P(n)$, which is its value in a completely polarized (magnetized) electron gas, and $\varepsilon_{xc}^U(n)$, the value for an unpolarized gas. For computational convenience, the variable $m_z(\mathbf{r})$ is replaced by:

$$\zeta = \frac{m_z}{n} = \frac{(n_\uparrow - n_\downarrow)}{(n_\uparrow + n_\downarrow)}. \tag{1.14}$$

One finally obtains:

$$\varepsilon_{xc}^{LSD}(n, \zeta) = \varepsilon_{xc}^U(n) + f(\zeta)[\varepsilon_{xc}^P(n) - \varepsilon_{xc}^U(n)], \tag{1.15}$$

where $f(\zeta)$ is a smooth interpolating function with f(0) = 0 and f(1) = 1.

The large majority of current DFT calculations on magnetic materials are based on this approximation. However, the study of nanomagnets requires a method to treat noncollinear magnetic systems, that is described in the next section, and the spin-orbit interaction must be included in the calculation, since it is responsible for the magnetic anisotropy which stabilizes magnetism in nanomagnets.

1.4 Beyond collinear spin magnetism

In the most general case, the energy of the system is a functional of the ground state charge-density $n(\mathbf{r})$ and of the three components of the magnetization density $\mathbf{m}(\mathbf{r})$.

In order to introduce the vector field $\mathbf{m}(\mathbf{r})$ in the formulation of DFT, one has to generalize the notion of Kohn-Sham orbitals. In the non-magnetic case, these orbitals are scalar functions. In the collinear magnetic case the orbitals are bi-dimensional spinors, for which one of the two components is zero, and is therefore not considered in the calculations. To describe a general magnetization density using one-particle wavefunctions, one has to resort to a representation with two-component spinors:

$$\boldsymbol{\psi}_i(\mathbf{r}) = \begin{pmatrix} \psi_{\uparrow i}(\mathbf{r}) \\ \psi_{\downarrow i}(\mathbf{r}) \end{pmatrix}. \tag{1.16}$$

In terms of these two-component spinors, the three components of the magnetization can be expressed as the expectation values of the Pauli matrices:

$$\mathbf{m}(\mathbf{r}) = \mu_B \sum_i^{occ} \boldsymbol{\psi}_i^+(\mathbf{r}) \boldsymbol{\sigma} \boldsymbol{\psi}_i(\mathbf{r}) = \mu_B \sum_i^{occ} \sum_{\alpha,\beta=1}^{2} \psi_{i\alpha}^*(\mathbf{r}) \boldsymbol{\sigma}_{\alpha\beta} \psi_{i\beta}(\mathbf{r}), \tag{1.17}$$

where μ_B is the Bohr magneton, and

$$\boldsymbol{\psi}_i^+(\mathbf{r}) = \begin{pmatrix} \psi_{\uparrow i}^*(\mathbf{r}), & \psi_{\downarrow i}^*(\mathbf{r}) \end{pmatrix}. \tag{1.18}$$

The components of the vector $\boldsymbol{\sigma}$ are the Pauli matrices:

$$\sigma_x = \begin{pmatrix} 0 & 1 \\ 1 & 0 \end{pmatrix};\ \sigma_y = \begin{pmatrix} 0 & i \\ -i & 0 \end{pmatrix};\ \sigma_z = \begin{pmatrix} 1 & 0 \\ 0 & -1 \end{pmatrix}. \tag{1.19}$$

The components of the magnetization in Eq. (1.17) read therefore:

$$\begin{aligned}
m_x(\mathbf{r}) &= \mu_B \sum_i^{occ} \boldsymbol{\psi}_i^+(\mathbf{r})\sigma_x\boldsymbol{\psi}_i(\mathbf{r}) = \mu_B \sum_i^{occ} \left(\psi_{i\uparrow}^*(\mathbf{r})\psi_{i\downarrow}(\mathbf{r}) + \psi_{i\downarrow}^*(\mathbf{r})\psi_{i\uparrow}(\mathbf{r})\right), \\
m_y(\mathbf{r}) &= \mu_B \sum_i^{occ} \boldsymbol{\psi}_i^+(\mathbf{r})\sigma_y\boldsymbol{\psi}_i(\mathbf{r}) = i\mu_B \sum_i^{occ} \left(\psi_{i\uparrow}^*(\mathbf{r})\psi_{i\downarrow}(\mathbf{r}) - \psi_{i\downarrow}^*(\mathbf{r})\psi_{i\uparrow}(\mathbf{r})\right), \\
m_z(\mathbf{r}) &= \mu_B \sum_i^{occ} \boldsymbol{\psi}_i^+(\mathbf{r})\sigma_x\boldsymbol{\psi}_i(\mathbf{r}) = \mu_B \sum_i^{occ} \left(\psi_{i\uparrow}^*(\mathbf{r})\psi_{i\uparrow}(\mathbf{r}) - \psi_{i\downarrow}^*(\mathbf{r})\psi_{i\downarrow}(\mathbf{r})\right).
\end{aligned} \tag{1.20}$$

The charge-density becomes:

$$n(\mathbf{r}) = \sum_i^{occ} \left(\boldsymbol{\psi}_i^+(\mathbf{r})\boldsymbol{\psi}_i(\mathbf{r})\right) = \sum_i^{occ} \psi_{i\uparrow}^*(\mathbf{r})\psi_{i\uparrow}(\mathbf{r}) + \psi_{i\downarrow}^*(\mathbf{r})\psi_{i\downarrow}(\mathbf{r}). \tag{1.21}$$

As in the case of the usual Kohn-Sham wavefunctions, the spinors are constrained to be orthonormal:

$$\langle\boldsymbol{\psi}_i|\boldsymbol{\psi}_j\rangle = \int d\mathbf{r}\left(\psi_{i\uparrow}^*(\mathbf{r})\psi_{j\uparrow}(\mathbf{r}) + \psi_{i\downarrow}^*(\mathbf{r})\psi_{j\downarrow}(\mathbf{r})\right) = \delta_{ij}. \tag{1.22}$$

The non-interacting kinetic energy reads:

$$T = -\frac{\hbar^2}{2m}\sum_i^{occ}\int d\mathbf{r}\left(\psi_{i\uparrow}^*(\mathbf{r})\nabla^2\psi_{i\uparrow}(\mathbf{r}) + \psi_{i\downarrow}^*(\mathbf{r})\nabla^2\psi_{i\downarrow}(\mathbf{r})\right). \tag{1.23}$$

Traditionally, the exchange-correlation functionals $\varepsilon[n,\mathbf{m}]$ are analytically written, in an approximated form, as functionals of $n(\mathbf{r})$ and of the norm of $\mathbf{m}(\mathbf{r})$, $|\mathbf{m}(\mathbf{r})|$, where the $\varepsilon[n,|\mathbf{m}|]$ has the same expression than the one of the LSDA functionals, where $m_z(\mathbf{r})$ is replaced by $|\mathbf{m}(\mathbf{r})|$.

To derive the noncollinear KS equation one can make use of the variational principle:

$$\frac{\delta\varepsilon_{xc}(n,\mathbf{m})}{\delta\psi_{i\alpha}^*(\mathbf{r})} = V_{xc}(\mathbf{r})\psi_{i\alpha}(\mathbf{r}) + \sum_{j=1,3} B_{xc}(\mathbf{r})\sum_{\beta=1}^{2}\sigma_{j,\alpha\beta}\psi_{i,\beta}(\mathbf{r})\frac{\delta m_j}{\delta\psi_{i\alpha}^*}, \tag{1.24}$$

where $V_{xc}(\mathbf{r})$ and $B_{xc}(\mathbf{r})$ are respectively the exchange and correlation potential and the exchange and correlation magnetic field, defined as:

$$V_{xc} = \frac{\delta\varepsilon_{xc}(n,\mathbf{m})}{\delta n(\mathbf{r})}, \tag{1.25}$$

and

$$B_{xc,j} = \frac{\delta \varepsilon_{xc}(n, \mathbf{m})}{\delta m_j(\mathbf{r})}. \tag{1.26}$$

The noncollinear KS equation finally becomes:

$$\left(T + V_{ION}(\mathbf{r}) + V_H(\mathbf{r}) + V_{xc}(\mathbf{r}) + \mathbf{B}_{xc}(\mathbf{r}) \cdot \boldsymbol{\sigma}\right) \boldsymbol{\psi}_i(\mathbf{r}) = \varepsilon_i \boldsymbol{\psi}_i(\mathbf{r}). \tag{1.27}$$

The density and the three components of the magnetization are obtained solving the KS equations following an iterative procedure (see Ref. [24]).

The LSDA equations are a special case of the noncollinear ones, which applies when the magnetization is constrained to a unique direction in space. In LSDA only the z component of the magnetic field is taken to be different from 0, and the non diagonal terms of Eq. (1.27) vanish. This enables to describe the KS eigenstates using one particle wavefunctions instead of the bidimensional spinors, and to split Eq. (1.27) in two separate equations, one applied to wavefunctions with spin up, and the other applied to wavefunctions with spin down.

In 1988, Kübler and coworkers introduced a self-consistent method for calculating the electronic and magnetic properties of $\mathrm{RhMn_3}$, $\mathrm{PtMn_3}$, and other non-collinear systems [25]. In order to lift the constraint of collinearity, they introduced atomic spheres around every atom. The direction of the magnetization was then required to be constant inside every sphere, but spins in different spheres were allowed to have different directions. The directions of the magnetization for every atom were chosen so as to minimize the total energy. Inside every atomic sphere the wavefunctions were then required to be either spin-up or spin-down with respect to the given direction. The approximations on the shape of the potential and of the magnetic field are unnecessary limitations that were in fact overcome in the work of Nordström and Singh [26], of Oda, Pasquarello, and Car [27], and of Bylander, and Kleinman [28] who used a self consistent noncollinear calculation method.

This last method was used by Gebauer and Baroni [29] and applied to frustrated systems like the δ-phase of oxygen under pressure. An example of frustrated structure is reported in Fig. 1.2, illustrating three atoms in a triangular geometrical configuration interacting antiferromagnetically with each other. If the magnetic moments of this structure are constrained to lay

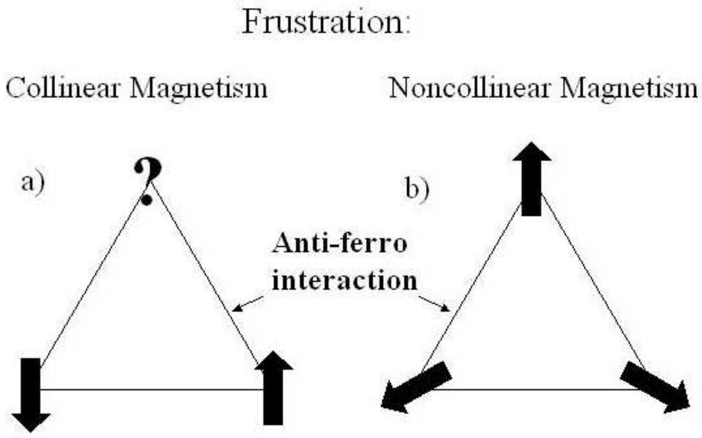

Figure 1.2: Frustrated magnetic system: a) Collinear magnetic ground state b) Noncollinear solution.

parallel to the z axis (like in (a)), only two of the three magnetic bonds can be satisfied. The noncollinear magnetic solution enables to overcome this problem and is displayed in (b). The study of the ground state properties of magnetic frustrated structures [29] or of magnetic excitations [30, 31, 32, 33] at finite temperature are not the only cases in which the noncollinear magnetism can be applied. Noncollinear spin arrangements may occur, for example, in the γ-phase of Fe which exhibits a spin-spiral structure [34, 35]. More generally, noncollinear configurations occur more easily in low symmetry or in disordered magnetic systems [36, 37], like small Fe clusters [27, 38], whose atoms are in a lower symmetry environment than in the bulk and are characterized by noncollinear spin arrangements.

1.4.1 A simple case study: iron clusters

As a preparation to the main goal of this thesis (i.e. the implementation of a fully relativistic version of noncollinear LSDA for calculating magnetic anisotropy) we performed a test calculation of the magnetic properties of a Fe_5 cluster using the methods of Ref. [39], as implemented by R. Gebauer and A. Dal Corso in the plane-wave QUANTUM-ESPRESSO code.

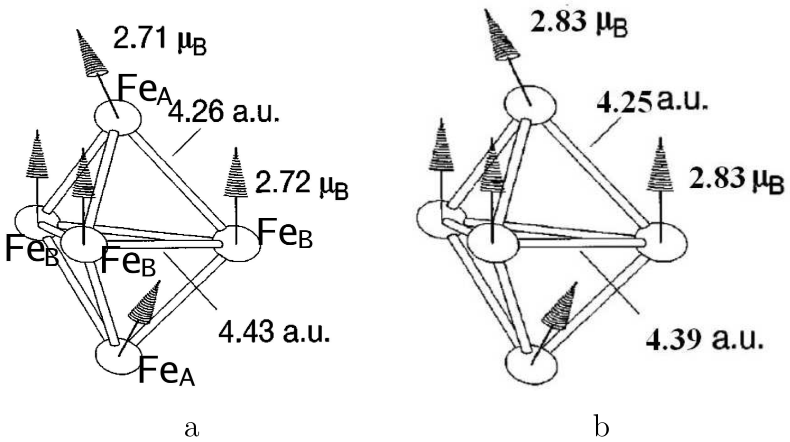

Figure 1.3: Inter-atomic distances and magnetic moments in the Fe_5 complex. In (a) the results of Ref. [27]. In (b), our results.

Magnetic properties

The magnetic properties of Fe_5 are reported and compared with those of

Table 1.1: Magnetic moments of the Fe atoms in the Fe_5 cluster. Comparison with the values reported in Ref. [27]. The magnetic moments of the apical (A) atoms and of the basal (B) atoms are reported in the first and second line respectively.

	This work	Ref [27]
Fe_A	(±1.72, 0.00, 2.24)	(±1.34, 0.00, 2.35)
Fe_B	(0.0, 0.00, 2.83)	(0.0, 0.00, 2.72)

Ref. [27] in table 1.1 and in Fig. 1.3. The magnetic moment of the apical and the basal atoms have almost the same absolute value, around 2.83 μ_B; the difference is of the order of 0.01 μ_B. They are instead different in direction: the basal atoms have their magnetic moments directed along the z axis (perpendicular to the base of the exahedron), while the magnetic moment of the apical Fe atoms forms with the z axis an angle of 37°. Ref. [27] has similar results: 2.72 μ_B for the absolute value of the magnetic moments, and the magnetic moments of the basal atoms is parallel to the z direction, while the apical atoms magnetic moments form an angle of 30° with the z axis.

Structural relaxation

The equilibrium atomic positions are shown in Fig. 1.3 and in table 1.2. The distance between the apical atoms (Fe_A) and the basal atoms (Fe_B, see Fig. 1.3) is smaller than the distance between the basal atoms. This is in agreement with the previous works found in literature ([27] and [40]). Also in these works a Perdew-Zunger functional has been used to describe the exchange-correlation interaction. All these results are summarized and compared with the results of Ref. [27] in Fig. 1.3.

Table 1.2: Calculated inter-atomic distances in the Fe_5 cluster and comparison with Refs. [27] and [40]. Fe_A-Fe_B indicates the distance between the apical atoms and the basal atoms while Fe_B-Fe_B indicates the distance between the basal atoms.

	This work	Ref [27]	Ref [40]
Fe_A-Fe_B [a.u.]	4.25	4.26	4.18
Fe_B-Fe_B [a.u.]	4.39	4.43	4.46

Computational details

The LSDA exchange-correlation functional is parametrized according to the formula given by Perdew and Zunger [18]. Periodic boundary conditions were adopted and the clusters were described with a simple cubic unit supercell having a lattice constant of 20 a.u., which is sufficient for the interactions between the periodic images to become negligible. An ultrasoft pseudopotential for the Fe atoms generated according to the modified Rappe-Rabe-Kaxiras-Joannopoulos scheme [41] with three Bessel functions was used. The spinor wavefunctions were expanded in a set of plane waves with a cutoff energy of 30 Ry. In the ultrasoft pseudopotential scheme [14] the density matrix has a hard augmented component, for which a cutoff energy of 300 Ry was used. The geometry optimization was initiated from the atomic configuration taken in a previous theoretical work [27]. The atomic coordinates were relaxed using Hellman-Feynman forces. The magnetic moments of each atom were estimated by integrating the magnetic density within non overlapping spheres of radius 1.75 a.u. centered on the atoms.

Chapter 2

Spin-orbit interaction and density functional theory

This chapter describes how the spin-orbit coupling can be included in electronic structure calculations based on plane waves and fully relativistic ultrasoft pseudopotentials. As a test I will present an application to the electron level splitting due to the spin-orbit in bulk Pt-fcc and Au-fcc.

2.1 Overview

The spin-orbit splitting of the electron energy levels is a relativistic effect due to the coupling of the intrinsic magnetic moment of the electron (proportional to its spin angular momentum) with the magnetic field induced by its orbital motion around the nucleus (proportional to the orbital angular momentum). In hydrogenic ions, spin-orbit splittings increase proportionally to Z^4, where Z is the nuclear charge. Simple qualitative arguments [42] show that, in many electron atoms, the spin-orbit splittings increase proportionally to $\approx Z^2$. More sophisticated estimations indicate that the Z dependence slightly changes according to the angular momentum of the atomic orbital considered [43]. As a consequence, in many-electron atoms, as the nuclear charge increases, the spin-orbit coupling becomes more and more effective so that, in heavy atoms, it is no more sufficient to deal with relativistic effects at the scalar relativistic level [44]. In solids containing heavy atoms the energy band structures are more sensitive to the spin-orbit interaction.

The spin-orbit is proportional to the fine structure constant $\alpha = e^2/\hbar c$. The eigenfunction of a non degenerate eigenstate of a scalar relativistic Hamiltonian are real, hence, treating the spin-orbit in perturbation theory, the first perturbative term would be purely imaginary, which is impossible. Hence, a non degenerate eigenstate, as well as the total energy of a system, and therefore also the MAE, are second order in α. One electron energy levels can instead be degenerate, and can therefore be first order in α.

In ab-initio calculations, spin-orbit effects can be explicitly included via the relativistic generalization of the Kohn and Sham (KS) equations, derived from relativistic density functional theory [45, 46]. The resulting equations are one-particle Dirac-like equations with a self-consistent potential. Examples of this approach are given in Ref. [47, 48]. A major contribution of the spin-orbit coupling to the valence-electron energies comes from the region close to the nuclei and can therefore be effectively included in the pseudopotentials (PPs). Relativistic effects up to order α^2 can be included in electronic structure calculations by solving non-relativistic KS equations with PPs tailored to reproduce the solutions of fully relativistic atomic Dirac-like equations [49].

2.2 Introduction of spin-orbit in the ultrasoft pseudopotential scheme

Relativistic PPs accounting for spin-orbit effects were introduced in semilocal form by Kleinman [49] and by Bachelet, and Schlüter [50]. Applications to solids, based on perturbation theory, could predict the spin-orbit splittings in the band structure of noble gas solids and simple semiconductors [51, 52]. In some cases the spin-orbit part of the PP has also been treated self-consistently by fully diagonalizing the relativistic Hamiltonian [53, 54]. More recently, the spin-orbit coupling has been treated by norm conserving PPs in fully separable form [55, 56], and spin-orbit split band structures of simple semiconductors and of magnetic solids such as MnAs and MnSe have been presented [57]. The ab-initio phonon dispersions of AuTe calculated including spin-orbit effects are also available [58].

We want now to include spin-orbit effects in the ultrasoft pseudopotentials (US-PPs) scheme [14]. US-PPs are employed extensively in large-scale electronic structure calculations because they allow precise and efficient simulations of systems containing localized $3d$ and $2p$ electrons, using plane-waves basis sets. In this scheme, the orbitals are allowed to be as soft as possible in the core regions but are subject to a generalized orthogonality constraint. The full charge is recovered by adding an augmentation charge localized in the core region to the square modulus of the orbitals. The implementation of spin-orbit coupling in ultrasoft pseudopotential (US-PPs) formalism will open the way to the study of nanomagnets, whose size is incompatible with the use of standard norm-conserving PPs.

2.2.1 Non local part of the fully-relativistic pseudopotentials

The radial components of the solutions of a fully relativistic atomic Dirac-like equation depend on the total angular momentum j and on the orbital angular momentum l. On the contrary, the radial components of the solutions of non relativistic (NR) or scalar relativistic (SR) [44] equations depend only on l. For $l > 0$, the solutions of the SR equation are "j-averaged" over the solutions of a fully relativistic equation, and the eigenvalues are not split by the spin-orbit coupling. There is a well known algorithm for the generation of US-PPs based on the solutions of NR or SR KS equations. The "j-averaged" US-PPs are generated by requiring that the scattering properties of the PP are exact at N_ε values of the energy for each l (usually $\mathrm{N}_\varepsilon \geq 2$). The coefficients of the resulting nonlocal PP form an l-dependent non-diagonal matrix $D^l_{\tau;\tau'}$ of dimensions $\mathrm{N}_\varepsilon \times \mathrm{N}_\varepsilon$ ($1 \leq \tau \leq \mathrm{N}_\varepsilon$). The symbol $D_{i,j}$, with two composite indexes $i \equiv \{\tau, l, m\}$ and $j \equiv \{\tau', l', m'\}$, often introduced in literature indicates $D_{\tau,l,m;\tau'l',m'} = D^{l\tau;\tau'}\delta_{l,l'}\delta_{m,m'}$, where m labels the projection of the orbital angular momentum on a quantization axis (-$l \leq m \leq l$). The nonlocal part of the PP is given by:

$$V^{PS} = \sum_I \sum_{\tau,l,m} \sum_{\tau',l',m'} D^{\gamma(I)}_{\tau,l,m;\tau',l',m'} |\beta^I_{\tau,l} Y^I_{l,m}\rangle \langle Y^I_{l',m'} \beta^I_{\tau',l'}|, \tag{2.1}$$

where the sum over I runs over the atoms of the system and $\gamma(I)$ identifies the atom type. For each l , $\beta^I_{\tau,l}$ are the N$_\varepsilon$ radial components of projector functions calculated together with the nonlocal PP coefficients [14]. $Y^I_{l,m}$ are the spherical harmonics, eigenfunctions of the one-electron orbital angular momentum. The index I means that these functions are centered about the atom I. V^{PS} is usually spin-independent because PPs generated from spin-unpolarized atomic configurations are often transferable enough to be used in magnetic materials within the local spin density approximation (LSDA) or the spin-dependent generalized gradient approximation (σ-GGA) [59, 60]. Even in fully unconstrained approaches to non-collinear magnetism [61, 62], V^{PS} is multiplied by the identity matrix in spin space before applying it to two-component spinor-wavefunctions.

Spin-orbit coupling can be included in a PP by taking, as reference all-electron wavefunctions, the large components of the solutions of a fully relativistic radial atomic Dirac-like equation [49]. For $l > 0$, there are solutions for $j = l + 1/2$ and for $j = l - 1/2$. For $l = 0$, there are solutions only for $j = 1/2$. Kleinman showed that, with a suitable potential, the NR KS equations can have solutions matching the large components of the solutions of a Dirac-like equation up to order α^2 [49]. An US-PP that accounts for spin-orbit coupling can be constructed following the standard algorithm, requiring that the scattering properties of the PP are exact at N_ε values of the energy for l and j. The coefficients of the nonlocal PP will form an l and j dependent matrix $D^{l,j}_{\tau;\tau'}$ of dimension N_ε x N_ε. In analogy with the "j-averaged" US-PPs, we introduce the notation $D_{\tau,l,j,m_j;\tau',l',j',m'_j} = D^{l,j}_{\tau;\tau'}\delta_{l,l'}\delta_{j,j'}\delta_{m_j,m'_j}$ where $(-j \leq m_j \leq j)$ labels the projection of the one-electron total angular momentum on a fixed quantization axis. The non-local PP is a 2×2 matrix of operators acting on two-component spinor wavefunctions. The local potential can be chosen as in a "j-averaged" US-PP and the components of the non-local part of the PP are:

$$V^{PS,\sigma,\sigma'}_{with\ s.o.} = \sum_I \sum_{\tau,l,j,m_j} \sum_{\tau',l',j',m'_j} D^{\gamma(I)}_{\tau,l,j,m_j;\tau',l',j',m'_j} |\beta^I_{\tau,l,j}\tilde{Y}^{\sigma,I}_{l,j,m_j}\rangle\langle\tilde{Y}^{\sigma',I}_{l',j',m'_j}\beta^I_{\tau',l',j'}|, \tag{2.2}$$

where $\beta^I_{\tau,l,j}$ are the N_ε radial components of the projector functions obtained together with the PPs coefficients for each l and j, and $\tilde{Y}^{\sigma,I}_{l,j,m_j}$ are the spin-angle functions, eigenfunctions of the total angular momentum, and of the square of the orbital and of the spin angular momenta. Fully separable norm-conserving PPs including spin-orbit effects were introduced also in Refs [55] and [56]. These PPs are special cases of Eq.(2.2), with $N_\varepsilon = 1$.

For the implementation of Eq. (2.2) in an electronic structure code, it is helpful to show that $V^{PS,\sigma,\sigma'}_{with s.o.}$ can be rewritten as Eq. (2.1) and hence it can be applied to each component of a spinor wavefunction as a "j-averaged" US-PP where the number of projector functions is twice as large for each $l > 0$, and the PP's coefficients are, in general, complex and depend on σ and σ'. In order to prove this result and to write an explicit expression for the PP's coefficients, we need to define a few quantities. We start by recalling that for $j = l + 1/2$, the spin-angle functions $\tilde{Y}_{l,j,m_j}$ are:

$$\tilde{Y}_{l,j,m_j} = \begin{pmatrix} \left(\frac{l+m+1}{2l+1}\right)^{1/2} Y_{l,m} \\ \left(\frac{l-m}{2l+1}\right)^{1/2} Y_{l,m+1} \end{pmatrix}, \tag{2.3}$$

where $m = m_j - 1/2$, while for $j = l - 1/2$, the spin angle functions $\tilde{Y}_{l,j,m_j}$ are:

$$\tilde{Y}_{l,j,m_j} = \begin{pmatrix} \left(\frac{l-m+1}{2l+1}\right)^{1/2} Y_{l,m-1} \\ -\left(\frac{l+m}{2l+1}\right)^{1/2} Y_{l,m} \end{pmatrix}, \tag{2.4}$$

where $m = m_j + 1/2$. In these two equations, the spherical harmonics have the complex form as those in Eq. (2.1). However, Eq. (2.1) is invariant, in form, for unitary transformations of the spherical harmonics: in particular, it remains valid for both the real and the complex forms. To keep the same generality in the final expressions, we introduce the $(2l + 1) \times (2l + 1)$ unitary matrix $U^l_{m,m'}$ which rotates the spherical harmonics at the same l and transforms the real form of the spherical harmonics, $Y'_{l,m}$, to the complex form,

$$Y_{l,m} = \sum_{m'=-l}^{l} U^l_{m,m'} Y'_{l,m'}, \tag{2.5}$$

The explicit expression of the U matrix elements is reported in appendix A together with the Clebsch-Gordan coefficients $\alpha^{\sigma,l,j}_{m_j}$. By using these definitions, each component of a spin-angle function can be written in a compact form as:

$$\tilde{Y}^{\sigma}_{l,j,m_j} = \alpha^{\sigma,l,j}_{m_j} \sum_{m'=-l}^{l} U^{\sigma,l,j}_{m_j,m'} Y'_{l,m'}. \tag{2.6}$$

The matrix elements of the nonlocal PP are therefore

$$V^{PS,\sigma,\sigma'}_{with\,s.o.} = \sum_{I} \sum_{\tau,l,j,m} \sum_{\tau',l',j',m'} D^{\gamma(I),\sigma,\sigma'}_{\tau,l,j,m;\tau',l',j',m'} |\beta^{I}_{\tau,l,j} Y'^{I}_{l,m}\rangle \langle Y^{I}_{l',m'} \beta^{I}_{\tau',l',j'}|, \tag{2.7}$$

where

$$D^{\gamma(I),\sigma,\sigma'}_{\tau,l,j,m;\tau',l',j',m'} = D^{\gamma(I),l,j}_{\tau;\tau'} f^{\sigma,\sigma'}_{l,j,m;l,j,m'} \tag{2.8}$$

and $f^{\sigma,\sigma'}_{l,j,m;l,j,m'}$ indicates the particular combination of Clebsch-Gordan coefficients and $U^{\sigma,l,j}_{m_j,m}$ matrix elements given by:

$$f^{\sigma,\sigma'}_{l,j,m;l,j,m'} = \sum_{m_j=-j}^{j} \alpha^{\sigma,l,j}_{m_j} U^{\sigma,l,j}_{m_j,m} \alpha^{\sigma',l,j}_{m_j} U^{*\sigma',l,j}_{m_j,m'}. \tag{2.9}$$

The special symbols $f^{\sigma,\sigma'}_{l,j,m;l,j,m'}$ have been introduced because the same combinations also appear in some of the expressions to follow. In Eq. (2.7), $-l \leq m \leq l$ and $-l' \leq m' \leq l'$ as in Eq. (2.1), so that each component $V^{PS,\sigma,\sigma'}_{sl,with\,s.o.}$ can be applied to component of spinor wavefunction as V^{PS}. Differently from Eq. (2.1), in Eq. (2.7), the coefficients $D^{\gamma(I),\sigma,\sigma'}_{\tau,l,j,m;\tau',l,j,m'}$ are non-diagonal in the indexes m, m'. This fact does not introduce any difficulty because also the "screened" coefficients (see below) of a standard US-PP are non-diagonal. Eq. (2.7) is valid for any combination of spherical harmonics provided that the U matrix in Eq. 2.5 is explicitly retained in the $D^{\gamma(I),\sigma,\sigma'}_{\tau,l,j,m;\tau',l',j',m'}$ coefficients, as in Eq. (2.7). Actually, the price to pay for using the real form of the spherical harmonics is the introduction of complex PP coefficients. It is well known that semi-local PPs written in terms of spin-angle functions can be recast in terms of spherical harmonics [49, 50]. Fully separable norm-conserving PPs with spin-orbit can also been rewritten in terms of spherical harmonics instead of spin-angle functions as shown in Ref. [55] (see Eq. (9) of this reference). Our Eq. (2.7) is the generalization of Eq. (9) of Ref. [55]. Moreover, our expression is valid for any unitary transformation among spherical harmonics.

2.2.2 Augmentation charge and orthogonality

When fully separable norm-conserving PPs are used, the description of spin-orbit coupling within a scheme for unconstrained non-collinear magnetism requires only the charge of the nonlocal PP coefficients described by Eq. (2.8). In this case our approach is totally equivalent to that of Ref. [56]. In order to employ US-PPs, the following points have still to be described: (i) the augmentation term in the charge and magnetization densities, (ii) the generalized orthogonality constraint satisfied by the spinor wavefunctions and (iii) the screening due to the charge-density augmentation, which are added to the coefficients of the nonlocal PP in the KS equations.

i) Charge and magnetization densities: we calculate the magnetization density by exploiting the similarity between the Projector augmented-wave (PAW) method introduced by P. Blöchl [63] and the US-PP's formalism. When non-collinear magnetic interactions are accounted for, DFT can be expressed in terms of a 2×2 density matrix $n^{\sigma,\sigma'}(\mathbf{r})$. The density matrix, written in terms of the all-electron two-components spinor wavefunctions $|\tilde{\psi}^{AE}_{\mathbf{k},v}\rangle$ is given by:

$$n^{\sigma,\sigma'}(\mathbf{r}) = \sum_{\mathbf{k},v} f_{\mathbf{k},v} \langle \tilde{\psi}^{\sigma,AE}_{\mathbf{k},v}|\mathbf{r}\rangle\langle\mathbf{r}|\tilde{\psi}^{\sigma',AE}_{\mathbf{k},v}\rangle, \tag{2.10}$$

where the sum is over a uniform mesh of $\mathbf{k}$ points in the Brillouin zone, and on the all bands at each point, and $f_{\mathbf{k},v}$ are the occupation factors [64]. The electron density is the trace of the density matrix $n(\mathbf{r}) = \sum_\sigma n^{\sigma,\sigma}(\mathbf{r})$, while the magnetization density is: $\mathbf{m}(\mathbf{r}) = \mu_B \sum_{\sigma,\sigma'} n^{\sigma,\sigma'}(\mathbf{r})\sigma^{\sigma,\sigma'}$, where σ are the Pauli matrices defined in Eq. 1.19 and μ_B is the Bohr magneton. The PAW formalism allows us to write the all-electron two-component spinor wavefunctions in terms of the two-components pseudo spinor wavefunctions $|\tilde{\psi}^{PS}_{\mathbf{k},v}\rangle$ and the all-electron and pseudo partial waves calculated in the isolated atoms. Spinor partial waves must be used to account for spin-orbit coupling and the linear transformation that maps valence pseudowavefunctions into all-electron wavefunctions becomes:

$$\begin{aligned}|\tilde{\psi}^{\sigma,AE}_{\mathbf{k},v}\rangle =& |\tilde{\psi}^{\sigma,PS}_{\mathbf{k},v}\rangle + \sum_I \sum_{\tau,l,j,m_j} \left[|\phi^{I,AE}_{\tau,l,j} \tilde{Y}^{\sigma,I}_{l,j,m_j}\rangle - |\phi^{I,PS}_{\tau,l,j} \tilde{Y}^{\sigma,I}_{l,j,m_j}\rangle \right] \times \\ & \sum_{\sigma_1} \langle \tilde{Y}^{\sigma_1,I}_{l,j,m_j} \beta^I_{\tau,l,j} | \tilde{\psi}^{\sigma_1,PS}_{\mathbf{k},v}\rangle.\end{aligned} \tag{2.11}$$

Here $\phi^{I,AE}_{\tau,l,j}(r)$ and $\phi^{I,PS}_{\tau,l,j}(r)$ are the radial components of the all-electron and pseudo partial waves, respectively. Inserting Eq. (2.11) into Eq. (2.10), we obtain the density matrix as:

$$\begin{aligned}
n^{\sigma,\sigma'}(\mathbf{r}) = &\sum_{\mathbf{k},v} f_{\mathbf{k},v}[\langle\tilde{\psi}^{\sigma,PS}_{\mathbf{k},v}|\mathbf{r}\rangle\langle\mathbf{r}|\tilde{\psi}^{\sigma',PS}_{\mathbf{k},v}\rangle + \\
&\sum_{I}\sum_{\tau,l,j,m_j}\sum_{\tau',l',j',m'_j}\sum_{\sigma_1,\sigma_2}\langle\tilde{\psi}^{\sigma_1,PS}_{\mathbf{k},v}|\beta^{I}_{\tau,l,j}\tilde{Y}^{\sigma_1,I}_{l,j,m_j}\rangle\times \\
&(\langle\tilde{Y}^{\sigma,I}_{l,j,m_j}\phi^{I,AE}_{\tau,l,j}|\mathbf{r}\rangle\langle\mathbf{r}|\phi^{I,AE}_{\tau',l',j'}\tilde{Y}^{\sigma',I}_{l',j',m'_j}\rangle - \\
&\langle\tilde{Y}^{\sigma,I}_{l,j,m_j}\phi^{I,PS}_{\tau,l,j}|\mathbf{r}\rangle\langle\mathbf{r}|\phi^{I,PS}_{\tau',l',j'}\tilde{Y}^{\sigma',I}_{l',j',m'_j}\rangle)\times \\
&\langle\tilde{Y}^{\sigma_2,I}_{l',j',m'_j}\beta^{I}_{\tau',l',j'}|\tilde{\psi}^{\sigma_2,PS}_{\mathbf{k},v}\rangle].
\end{aligned} \tag{2.12}$$

We now use Eq. (2.6) for the component of the spin-angle functions and introduce augmentation functions in close analogy with the "j-averaged" US-PPs.

$$\begin{aligned}
&Q^{I}_{\tau,l,j,m;\tau',l',j',m'}(\mathbf{r}) = \\
&\qquad\left[\phi^{I,AE}_{\tau,l,j}(r)\phi^{I,AE}_{\tau',l',j'}(r) - \phi^{I,PS}_{\tau,l,j}(r)\phi^{I,PS}_{\tau',l',j'}(r)\right] Y'^{*,I}_{l,m}(\Omega)Y'^{I}_{l',m'}(\Omega),
\end{aligned} \tag{2.13}$$

where (r,Ω) are the spherical coordinates of $\mathbf{r}-\mathbf{R_I}$ ($\mathbf{R_I}$ is the position of atom I). The density matrix becomes:

$$\begin{aligned}
n^{\sigma,\sigma'}(\mathbf{r}) = &\sum_{\mathbf{k},v} f_{\mathbf{k},v}\langle\tilde{\psi}^{\sigma,PS}_{\mathbf{k},v}|\mathbf{r}\rangle\langle\mathbf{r}|\tilde{\psi}^{\sigma',PS}_{\mathbf{k},v}\rangle + \\
&\sum_{I}\sum_{\tau,l,j,m_j}\sum_{\tau',l',j',m'_j} Q^{I}_{\tau,l,j,m;\tau',l',j',m'}(\mathbf{r})\rho^{I,\sigma,\sigma'}_{\tau,l,j,m;\tau',l',j',m'},
\end{aligned} \tag{2.14}$$

where:

$$\begin{aligned}
\rho^{I,\sigma,\sigma'}_{\tau,l,j,m;\tau',l',j',m'} = &\sum_{\mathbf{k},v} f_{\mathbf{k},v}(\sum_{\sigma_1}\sum_{m_1} f^{\sigma_1,\sigma}_{l,j,m_1;l,j,m}\langle\tilde{\psi}^{\sigma_1,PS}_{\mathbf{k},v}|\beta^{I}_{\tau,l,j}Y'^{I}_{l,m_1}\rangle\times \\
&\sum_{\sigma_2}\sum_{m_2} f^{\sigma',\sigma_2}_{l',j',m';l',j',m_2}\langle Y'^{I}_{l',m_2}\beta^{I}_{\tau',l',j'}|\tilde{\psi}^{\sigma_2,PS}_{\mathbf{k},v}\rangle).
\end{aligned} \tag{2.15}$$

Despite the apparent complexity, the calculation of these terms is as difficult as the standard calculation of the density matrix since Eq. (2.14) has the same form of the "j-averaged" formula [14]. After the calculation of the scalar products between two-component spinor wavefunctions and projector-functions, the number of operations to make the sum over σ_1 and m_1 (or σ_2 and m_2), is negligible. The computational overhead is due only to the higher number of projector functions.

ii) Generalized orthogonality constraint: the integral of the electron charge-density has to be equal to the number of electrons. this condition is fulfilled if the two-component spinor wavefunctions are subject to a generalized orthogonality constraint consistent with the augmentation term in the density matrix. Using Eq. (2.14), we find that spinors must obey the generalized orthogonality constraint: $\langle\tilde{\psi}^{PS}_{\mathbf{k},v}|S|\tilde{\psi}^{PS}_{\mathbf{k},v'}\rangle = \delta_{v,v'}$, where S is a 2×2 overlap matrix whose elements are given by:

$$S^{\sigma,\sigma'} = \sum_{I} \sum_{\tau,l,j,m} \sum_{\tau',l',j',m'} q^{\gamma(I),\sigma,\sigma'}_{\tau,l,j,m;\tau',l',j',m'} |\beta^{I}_{\tau,l,j} Y'^{I}_{l,m}\rangle\langle Y'^{I}_{l',m'}|\beta^{I}_{\tau',l',j'}|. \tag{2.16}$$

Each element of S has the same form of the S matrix of a "j-averaged" US-PP, with coefficients $q^{\gamma(I),\sigma,\sigma'}_{\tau,l,j,m;\tau',l',j',m'}$ that, in general, are complex and depend on σ and σ':

$$q^{\gamma(I),\sigma,\sigma'}_{\tau,l,j,m;\tau',l',j',m'} = \sum_{m_1,m_2} \sum_{\sigma_1} q^{\gamma(I)}_{\tau,l,j,m_1;\tau',l',j',m_2} f^{\sigma,\sigma_1}_{l,j,m;l,j,m_1} f^{\sigma_1,\sigma'}_{l',j',m_2;l',j',m'}. \tag{2.17}$$

Here $q^{\gamma(I),\sigma,\sigma'}_{\tau,l,j,m;\tau',l',j',m'} = \int d\mathbf{r} Q^{\gamma(I),\sigma,\sigma'}_{\tau,l,j,m;\tau',l',j',m'}(\mathbf{r})$ are the integrals of the augmentation functions, Eq. (2.13), while $f^{\sigma,\sigma'}_{l,j,m;l,j,m'}$ are defined by Eq. (2.9).

iii) D coefficients of the nonlocal PP: The total energy is a functional of the density matrix and can be written for two-component spinor wavefunctions with the local US-PP given by Eq. (2.7). The minimization of this energy functional with respect to the spinor wavefunctions yields the KS equations. Since the augmentation terms in the density matrix depend on the spinor wavefunctions, additional terms appear in KS equations. These terms can be included in the nonlocal PP by screening the D coefficients [14].

In analogy with "j-averaged" US-PPs, we get:

$$\begin{aligned}\tilde{D}^{I,\sigma,\sigma'}_{\tau,l,j,m;\tau',l',j',m'} =& D^{\gamma(I),\sigma,\sigma'}_{\tau,l,j,m;\tau',l',j',m'} + \\ & \sum_{m_1,m_2} \sum_{\sigma_1,\sigma_2} \sum_{\alpha} \mathbf{A}^{\sigma_1,\sigma_2}_{\alpha} \mathbf{I}^{I,\alpha}_{\tau,l,j,m_1;\tau',l',j',m_2} f^{\sigma,\sigma_1}_{l,j,m;l,j,m_1} f^{\sigma_2,\sigma'}_{l',j',m_2;l',j',m'},\end{aligned} \tag{2.18}$$

where $\mathbf{A}$ is a four-component vector ($1 \leq \alpha \leq 4$) of 2×2 matrix: $\mathbf{A} = (\mathbf{1}, \sigma_x, \sigma_y, \sigma_z)$ ($\mathbf{1}$ is the 2×2 identity matrix, and σ_i are the Pauli matrices). $\mathbf{I}^{I,\alpha}_{\tau,l,j,m;\tau',l',j',m'} = \int d\mathbf{r} Q^{I}_{\tau,l,j,m;\tau',l',j',m'}(\mathbf{r})\mathbf{B}_{\alpha}(\mathbf{r})$ are the integrals of the product of the augmentation function with either the effective potential V_{eff} or the exchange and correlation magnetic field. The four component vector $\mathbf{B}$ is defined as $\mathbf{B} = (V_{eff}, -\mu_B B_{xc,x}, -\mu_B B_{xc,y}, -\mu_B B_{xc,z})$, where the effective potential V_{eff} is the sum of the local, Hartree and exchange and correlation potentials, while the exchange and correlation magnetic field is the functional derivative of the exchange and correlation energy E_{xc} with respect to the magnetization: $B_{xc,i} = -\frac{\delta E_{xc}}{\delta m_i}$. In summary, Eqs. (2.17) (2.18) (2.16) and (2.15) show how to account for the spin-orbit coupling by a fully relativistic US-PP. In the next section, I will present applications of this formalism to the calculation of the structural and electronic properties of bulk fcc-Au and of fcc-Pt.

2.3 Application to Au-fcc and Pt-fcc

For Fe, Co, and Ni cubic crystals [65], the magnetic anisotropy energy (MAE) is of the order of the μeV per unitary cell. For the hexagonal Co lattice, the MAE is of the order of 0.1 meV. 2D and 1D-systems are more sensitive to the anisotropic effects because the charge-density has a sharp distribution in some directions (where it goes to zero very soon), and a smooth distribution in other directions (where it obeys to periodic conditions). In such magnetic systems the MAE is usually of the order of some meV.

Nevertheless the fact that 3D-lattices are less sensitive to the anisotropic effects than other systems does not mean that their electronic structure is not affected by the spin-orbit term. This is more clear in the illustrative case of the hydrogen atom: the system is perfectly isotropic and the MAE is zero, but the energy levels are split because of the spin-orbit interaction.

As discussed previously, the splitting of the bands are more evident in solids composed of atoms with a large nuclear charge, like, for example, Au and Pt. These are therefore suitable systems to verify if the fully relativistic US-PPs applied within a DFT scheme based on two-component spinor wavefunctions can reproduce the band structures and the structural properties as predicted by a fully relativistic four-component Dirac-like equation. I will therefore focus on the structure and electronic properties of these two 3D non magnetic systems.

2.3.1 Computational details

US-PPs for Au and Pt were generated according to the modified Rappe-Rabe-Kaxiras-Joannopoulos scheme [41] with three Bessel functions. We used as reference all-electron configuration $5d^4_{3/2}5d^4_{5/2}6s^2_{1/2}$ and $5d^4_{3/2}5d^6_{5/2}6s^1_{1/2}$ for Pt and Au, respectively. The core radii (in a.u.) of our pseudopotentials are: Pt $5d$ (2.1, 2.4), $6p_{1/2}$ (3.3), $6p_{3/2}$ (3.4). The potential of the s channel was taken as local with $r_{loc} = 2.6$. Au $5d$ (1.8, 2.4), $6p$ (3.3). The potential of the s channel was taken as local with $r_{loc} = 2.7$. Two values of the core radii indicate a channel which was pseudized with the US scheme. In such case, the first value is the norm conserving core radius and the second is the ultrasoft one. The same core radii were taken for the $j = l + 1/2$ and $j = l - 1/2$ channels when not explicitly specified. The same radii were used also for the SR PPs.

The all-electron reference atomic radial wavefunctions were calculated by solving a relativistic Dirac-like equation within the local density approximation (LDA) for the exchange and correlation energy and the Perdew and Zunger [18] parametrization. The non linear core correction [66] (NLCC) with $r_{core} = 1.2$ a.u. was used to obtain a non-magnetic ground state for fcc-Pt. A kinetic energy cutoff of 30 Ry was used for the plane-waves expansion of the pseudo-wavefunctions (250 Ry for the charge densities), a $8 \times 8 \times 8$ Monkhorst-Pack mesh [67] of special points for the integration over the Brillioun zone and the smearing approach of Ref. [64] for dealing with the Fermi surface. The smearing parameter was 0.02 Ry for both Au and Pt.

2.3.2 Structural and electronic properties

The values of the equilibrium lattice constants and bulk moduli calculated with our US-PPs are reported in Tab. 2.1 and compared with the values reported in the literature, with experiment and with results obtained by "j-averaged" US-PPs constructed by starting from the solutions of a SR atomic equation. First of all, we note that the introduction of spin-orbit coupling does not change significantly the structural properties. The lattice constants calculated with or without spin-orbit coupling differ by less than 0.02 a.u., while the Bulk moduli change by a few percent. We find very good agreement with previous all-electron calculations, for the lattice constant of Au, whereas the lattice constant of Pt is overestimated by about 0.5%. The bulk moduli are correct within a few percent. These errors are within the accuracy of our PPs.

Table 2.1: Theoretical lattice constant and bulk modulus of the systems studied in this work compared with previous calculations and with experiments. SO indicates a fully relativistic US-PP, while SR indicates a "j-averaged" US-PP.

	fcc-Pt		fcc-Au	
	a$_0$ (a.u.)	B$_0$ (kbar)	a$_0$ (a.u.)	B$_0$ (kbar)
This work (SO)	7.40	2920	7.64	1981
This work (SR)	7.39	2953	7.65	1924
Ref. [68]	7.37	2970	7.637	1950
Ref. [48]	7.36	2950	7.638c	1975
Expt.	7.40[a],7.414[b]	2830[a]	7.67[a],7.707[b]	1730[a]

[a] Ref. [69]

[b] Ref. [70], used in Ref. [68]

[c] Obtained with NR exchange-correlation functional

In Figs. 2.1 and 2.2, the electronic band structures of fcc-Pt and fcc-Au are reported along several symmetry lines of the Brillouin zone, calculated at the experimental lattice constant extrapolated at zero temperature [69]: $a_0 = 7.40$ a.u. (Pt) and $a_0 = 7.67$ a.u. (Au).

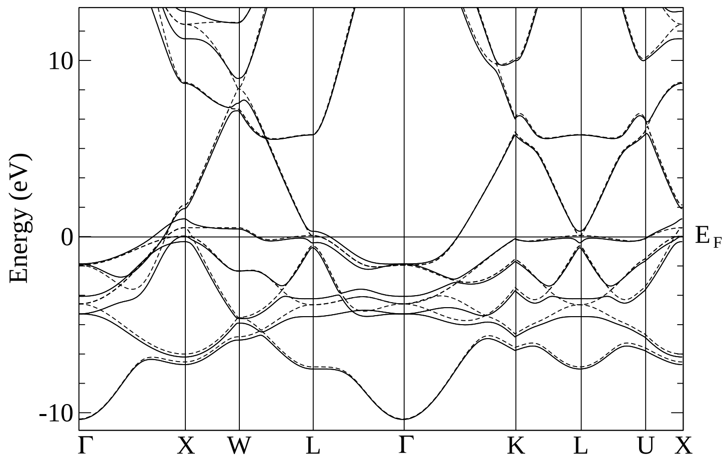
fcc-Pt

Figure 2.1: fcc-Pt band structure calculated with scalar relativistic pseudopotentials (dashed line) and with relativistic pseudopotential (continuous line).

Figs. 2.1 and 2.2 also show the comparison between fully relativistic and scalar relativistic electronic band structures of fcc-Pt and fcc-Au calculated at the experimental lattice constant. The largest energy splittings (around 1 eV) due to the spin-orbit coupling are at the Γ point. A deeper analysis of the energy eigenvalues calculated at the Γ, X, W, L and K points is reported in Tab. 2.2 where our results are compared with those calculated in Ref. [68] and in Ref. [48]. In Ref. [68], the band structures are the eigenvalues of a relativistic full-potential Dirac-like equation solved by the Korringa-Kohn-Rostoker method, whereas Ref. [48] reports the eigenvalues of a Dirac-like equation solved by an augmented plane wave (APW) method and assuming a spherical symmetric crystal potential inside the APW spheres. Both calculations were carried out within DFT in the LDA with two different parameterizations of the functional: the Hedin and Lundqvist [71] form in Ref. [68] and the Vosko *et al.* [72] for in Ref. [48]. In Ref. [48], relativistic corrections to the *fcc*-Au

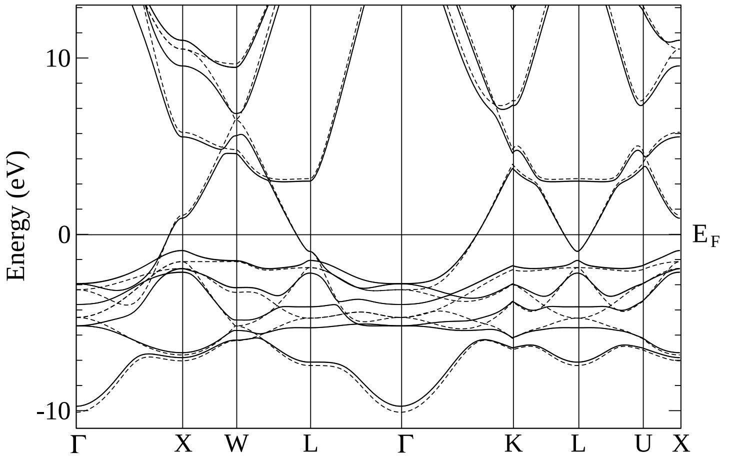

Figure 2.2: *fcc*-Au band structure calculated with scalar relativistic pseudopotentials (dashed line) and with relativistic pseudopotential (continuous line).

exchange and correlation energy were also introduced but the changes due to these functionals were found to be small. The reference values reported in Tab. 2.2 were extrapolated from Fig. 2 of Ref. [68] and from Figs. 1 and 3 of Ref. [48]. We estimated and quoted two significant digits, but the errors introduced by this procedure are of the order of 0.1 eV. In Ref. [68], the band structure calculations are done at the room-temperature experimental lattice constants, while we could not find the lattice constants used in Ref. [48]. In order to check our method against these data, we calculated the band structures at three lattice constants: in addition to the zero-temperature experimental lattice constants we considered also $a_0 = 7.414$ a.u. (Pt) and $a_0 = 7.707$ a.u. (Au), the room-temperature experimental lattice constants used in Ref. [68], and $a_0 = 7.36$ a.u. (Pt) and $a_0 = 7.65$ a.u. (Au) the theoretical lattice constants found in Ref. [48].

For both Pt and Au, the lowest differences between our data and Ref. [68]

Table 2.2: Energy eigenvalues (expressed in eV) of the occupied states calculated at high-symmetry points of the Brillouin zone at the zero temperature experimental lattice constant. The calculated eigenvalues are compared with results available in literature, obtained by solving a four-component relativistic Dirac-like equation. The Fermi energy is taken as zero. In parenthesis our eigenvalues calculated at the lattice constant indicated in the first row.

	Pt	Pt[[48]]	Pt[[68]]	Au	Au[[48]]	Au[[68]]
a_0	7.40	? (7.36)	7.414 (7.414)	6.67	? (6.65)	6.707 (6.707)
Γ	-10.45	-10.56 (-10.63)	-10.35 (-10.39)	-10.18	-10.23 (-10.27)	-9.95 (-10.01)
	-4.38	-4.48 (-4.48)	-4.24 (-4.35)	-5.43	-5.41 (-5.49)	-5.32 (-5.35)
	-3.39	-3.47 (-3.49)	-3.28 (-3.35)	-4.23	-4.23 (-4.28)	-4.14 (-4.14)
	-1.53	-1.65 (-1.58)	-1.48 (-1.52)	-2.97	-3.04 (-3.01)	-2.96 (-2.92)
X	-7.28	-7.58 (-7.46)	-7.10 (-7.22)	-7.38	-7.53 (-7.46)	-7.14 (-7.23)
	-6.84	-6.99 (-7.01)	-6.70 (-6.78)	-7.08	-7.13 (-7.16)	-6.95 (-6.94)
	-0.25	-0.32 (-0.25)	-0.20 (-0.25)	-2.25	-2.24 (-2.26)	-2.27 (-2.22)
	0.06	0.05 (0.07)	0.04 (0.05)	-2.02	-1.98 (-2.03)	-2.07 (-2.01)
				-0.99	-0.92 (-0.99)	-1.03 (-0.98)
W	-5.89	-6.19 (-6.04)	-5.72 (-5.84)	-6.32	-6.47 (-6.40)	-6.16 (-6.21)
	-4.93	-5.01 (-5.04)	-4.83 (-4.89)	-5.72	-5.81 (-5.78)	-5.67 (-5.63)
	-4.67	-4.80 (-4.79)	-4.58 (-4.62)	-5.16	-5.22 (-5.22)	-5.08 (-5.05)
	-1.95	-2.13 (-2.00)	-1.87 (-1.93)	-3.21	-3.30 (-3.25)	-3.20 (-3.15)
				-1.57	-1.58 (-1.58)	-1.62 (-1.56)
L	-7.54	-7.68 (-7.71)	-7.44 (-7.48)	-7.62	-7.66 (-7.71)	-7.53 (-7.48)
	-4.54	-4.69 (-4.64)	-4.43 (-4.49)	-5.55	-5.61 (-5.61)	-5.52 (-5.46)
	-3.52	-3.68 (-3.62)	-3.45 (-3.49)	-4.36	-4.42 (-4.42)	-4.33 (-4.28)
	-0.76	-0.85 (-0.83)	-0.79 (-0.74)	-2.30	-2.31 (-2.31)	-2.37 (-2.27)
	-0.33	-0.37 (-0.32)	-0.30 (-0.33)	-1.57	-1.58 (-1.59)	-1.62 (-1.55)
				-1.18	-1.25 (-1.23)	-1.23 (-1.10)
K	-6.47	-6.72 (-6.63)	-6.40 (-6.42)	-6.79	-6.86 (-6.86)	-6.70 (-6.66)
	-5.71	-5.87 (-5.85)	-5.57 (-5.66)	-6.18	-6.21 (-6.25)	-6.11 (-6.07)
	-3.10	-3.20 (-3.19)	-3.00 (-3.08)	-4.03	-4.09 (-4.08)	-4.04 (-3.95)
	-1.40	-1.60 (-1.43)	-1.38 (-1.38)	-2.96	-3.04 (-2.99)	-3.00 (-2.92)
	-0.10	-0.13 (-0.10)	-0.10 (-0.10)	-1.89	-1.91 (-1.91)	-1.97 (-1.86)

are found at the room temperature experimental lattice constants, whereas the lowest discrepancies with Ref. [48] are found at their theoretical lattice constant. In Au, a very good agreement between our calculations and the fully relativistic results is found, only the highest occupied band at L is 0.13 eV above that of Ref. [68], all other bands having errors lower than 0.1 eV. Also in Pt the agreement is quite good, almost always within 0.1 eV, with a few exceptions: the maximum error with respect to Ref. [68] is of 0.12 eV for the lowest band at X and W. The maximum error with respect to Ref. [48] is 0.17 eV for the fourth band at K, while the lowest bands at X and W differ by 0.12 and 0.15 eV, respectively.

In conclusion, it has been shown how to describe the spin-orbit coupling by fully relativistic US-PPs and that, for fcc-Au and fcc-Pt, these PPs, applied within a DFT scheme based on two-component spinor wavefunctions, can reproduce the band structures and the structural properties as predicted by a fully relativistic four-component Dirac-like equation.

Chapter 3

Magnetism in low-dimensional systems based on Cobalt

This chapter deals with 2D, 1D and 0D nanomagnets based on Co atoms. The structural, electronic, and magnetic properties, as well as the magnetic anisotropy energy, are calculated with the theoretical methods described in the previous chapters. The magnetic properties are shown to be extremely sensitive to the atomic geometries. The results are presented and compared with previous theoretical works and with the experiments by following an order of decreasing dimensionality.

In chapter 2 I have shown the importance of relativistic effects in the band structure of heavy transition metal atoms (Au and Pt) by applying the relativistic pseudopotential method. These systems are not magnetic and therefore not concerned in magnetic anisotropy phenomena. But even for other 3D systems that are magnetic, like for example Fe *bcc*, the MAE is typically very small, of the order of the μeV [65], and therefore not accessible by the present electronic structure calculations. The new method to compute the MAE needs to be benchmarked on systems in which the MAE is larger, like for example in low dimensional structures in which the MAE is of the order of some meV.

3.1 Methods for calculating the magnetic anisotropy energy

Before proceeding to the description of low dimensional systems, it is worth to give an overview of the methods currently used for the calculation of the MAE and to compare them with our method.

3.1.1 The force theorem

Many of the previous theoretical works are based on DFT all-electron calculations and the magnetic anisotropy is calculated on the basis of the force theorem [73]. The force theorem relates small changes in the total energy to changes in the eigenvalues upon variation of the angle between the direction of the total magnetization and the easy magnetization axis. We remark that, strictly speaking, this is not a "theorem" but an approximation, since it is valid only in the assumption that the charge-density is not modified by the changes in the magnetization direction. In this assumption, the change in energy is determined by the external potential only, not by the Hartree and exchange-correlation contributions. According to this theorem, the magneto-crystalline anisotropy energy can be approximated as the difference in band energies (the sum of the occupied eigenvalues) obtained with and without the spin-orbit coupling using the same self-consistent scalar-relativistic potential. Its usual "proof" takes advantage of the fact that the relativistic correction to the total energy is second order with respect to the differences in the charge and spin densities. The MAE is then given by the difference between the highest and the smallest band energies, identified by sampling systematically different directions of the total magnetization of a system.
In Ref. [74] the band energy of a Co nanowire on a (664) Pt surface is computed for different directions of the magnetic moment of the Co atoms and the applicability of the force theorem is checked for some configurations by comparison with self-consistent calculations. An average deviation of 0.2 meV/atom between the two methods is estimated, corresponding to 10% of the total MAE per unit cell.

3.1.2 Self consistent methods

Our approach goes beyond the force theorem since the MAE is calculated in terms of the self consistent total energy, not only in terms of the band energy. Our calculations are performed by the ultrasoft fully relativistic pseudopotential method described in the previous chapter. This method has proved to be a reliable scheme enabling to include spin-orbit in the solution of the KS equation. As stated previously, the spin-orbit term relates the electrons spin to the potential, and therefore is crucial for the calculation of the MAE. Ultrasoft fully relativistic pseudopotentials are therefore suitable to calculate the MAE. Furthermore, since pseudopotentials provide accurate predictions of the forces acting on the atoms, our method allows to study the effect of geometry optimization on the MAE.

The ground state of a magnetic system with magnetization laying parallel to the easy magnetization axis is evaluated selfconsistently. Even starting the calculation from different initial conditions with total magnetization direction different from that of the ground state, the system, during the calculation, evolves in such a way as to redirect its magnetization parallel to the easy magnetization axis. To evaluate the MAE, however, it is necessary to calculate the total energy in a magnetic configuration different from that of the ground state, in which the total magnetization lays parallel to the so called hard magnetization direction. The total magnetization can be constrained to lay along directions different from the equilibrium one. It is then possible to calculate the total energy in these magnetic configurations, and compare it with the ground state energy, obtaining in this way the MAE. During the calculation, however, the absolute value of the atomic magnetic moments, as well as their mutual directions, converge much faster than the total magnetization direction. The difference in energy between the configurations with magnetization directed along the easy and hard axis can be relevant in some systems, but our self consistent approach converges to the equilibrium configuration with a large number of iterations, where the total energy and the total magnetization direction change very slightly at each step. To calculate the properties of the system out of its equilibrium configuration it is therefore not necessary to constrain its total magnetization. It is sufficient to set the initial magnetization, and then to choose an energy convergency threshold sufficiently small to guarantee an accurate prediction of the absolute value of the atomic magnetic moments and their mutual direction, and sufficiently large to prevent the total magnetization to change direction from the initial condition. We therefore sample the total energy by varying the direction of the total magnetization, but, for each direction, the calculation is performed self consistently with the relativistic pseudopotentials. As a consequence our results are free from the approximation typical of the force theorem [74].

Other minor differences with respect to other theoretical works are in the inclusion of the spin-orbit interaction in the KS equation, and in the treatment of the magnetic dipole-dipole interaction. In our approach the spin-orbit contribution is accounted for in the nonlocal part of the pseudopotentials of the atoms involved, while in some previous works the spin-orbit interaction is taken into account by solving a Dirac-like KS-equation (fully relativistic calculation [75, 74, 76, 77]), in others by adding the spin-orbit term to the scalar relativistic Hamiltonian [78].

In some works [75, 79] the magnetic dipole-dipole energy is also added to the energy band for the calculation of the MAE. We computed the Co magnetic moments in the case of the unsupported Co monolayer and used them to calculate the magnetic dipole-dipole energy following Ref. [80]. We found a value of 0.08 meV, negligible with respect to the total MAE (2.0 meV). Therefore, since the magnetic dipole-dipole energy is more relevant in monolayers than in nanowires and adatoms, this term can be safely neglected in all the structures described in the following.

No relativistic effects are taken into account in the parameterizations of the exchange-correlation functional [72].

3.2 2D: Monolayers

The reduction of the dimensionality of a magnetic system from 3 to 2 induces a MAE increase of many orders of magnitude. Many recent studies focus on magnetic 2D systems and on their magnetic properties. In particular some works have been carried out on a Co monolayer deposited on a Au(111) surface [81]. Therefore, before studying 0D and 1D systems, I will begin by analyzing two systems in which the dimensionality is reduced to 2: an unsupported Co-monolayer and a Co-monolayer deposited on a Au(111) surface. In the case of the unsupported Co-monolayer, there are no experimental data available but theoretical studies have been carried out with the LMTO method, and ASA approximation [78]. For the Au-supported Co-monolayer instead our results can be compared with both theoretical methods [79] and experimental data [81].

3.2.1 Unsupported Co monolayer

Surface supported Co monolayers have been studied in several experimental works [81, 82]. The particular case of the Co monolayer on Au(111) surface has been recently analyzed, as well as the effect of additional overlayers on the MAE [81]. Our goal is to study first an isolated hexagonal Co monolayer, so as to understand the role of the supporting surface on the anisotropy of the system, sudied in the next section. Following Ref. [78], we performed the calculation for different in-plane lattice constants. In Ref. [78] the relativistic effects are taken into account by adding the spin-orbit term to the KS equation, and the MAE is calculated by the force theorem. According to our results and to Ref. [78], the easy magnetization axis is always parallel to the plane of the monolayer. Moreover we find that rotating the total magnetization in the monolayer plane results in energy changes below 0.01 meV, and the values of both the magnetic moment and of the total magnetization do not change upon rotation of the axis. The MAE and the Co spin magnetic moment increase for larger in-plane lattice constants, as reported in Table 3.1. Our results are in substantial good agreement with previous studies [78, 79], in which the MAE is calculated in LSDA, and considering the magnetic dipole-dipole energy contribution.

The Co spin magnetic moment calculated with the gradient-corrected PBE functional, is 2.07 μ_B, 5% larger than the LDA value (1.93 μ_B). In both cases it is smaller then the value for the free Co atom (3 μ_B). The MAE calculated with a gradient-corrected PBE exchange-correlation functional (0.67 meV) is also smaller than the LDA values (1.05 meV), but the easy magnetization axis is always parallel to the plane of the monolayer.

Table 3.1: MAE and Co spin magnetic moment computed with the relativistic pseudopotential method compared with results of Ref. [78]. Calculations are performed for different in-plane lattice constants: 4.74 a.u. (as in a (111) plane of hcp Co), 4.92 a.u., 5.15 a.u. (as in a (111) plane of fcc Pd).

a_0 [$a.u.$]		MAE	[meV]		μ_0	[μ_B]
	GGA	LDA	LDA (Ref. [78])	GGA	LDA	LDA (Ref. [78])
4.74	0.67	1.05	1.2	2.07	1.93	1.87
4.92	0.98	1.16	1.4	2.11	2.03	1.93
5.15	1.38	1.50	2.0	2.13	2.07	1.99

We deduce that, compared to LDA calculations, the PBE functional tends to disfavor configurations with the magnetization direction parallel to the monolayer.

3.2.2 Monolayer on the Au(111) surface

Several authors have discussed the peculiar magnetic properties of ultra-thin Co films supported by Au and Pt (111) surfaces. In particular Engel *et al.* [81] revealed that deposition of additional Ag, Cu, Au, or Pd layers increases significantly the perpendicular anisotropy. Further works revealed that the maximum increase of the MAE in the case of the Au(111) supported Co monolayer (0.5 meV) [82] is reached when a single Au-overlayer is added. We therefore restrict our study to this particular system displayed in Fig. 3.1. Differently from the unsupported Co monolayer, the easy magnetization axis is in this case perpendicular to the (111) plane and the experimental MAE is 0.6 meV [82]. From our theoretical calculations, performed on an unrelaxed surface structure, corresponding to an ideal truncation of a fcc crystal, we predict the same direction for the easy magnetization axis, but we obtain a larger value for the MAE (1.89 meV, see Table 3.2). Other theoretical

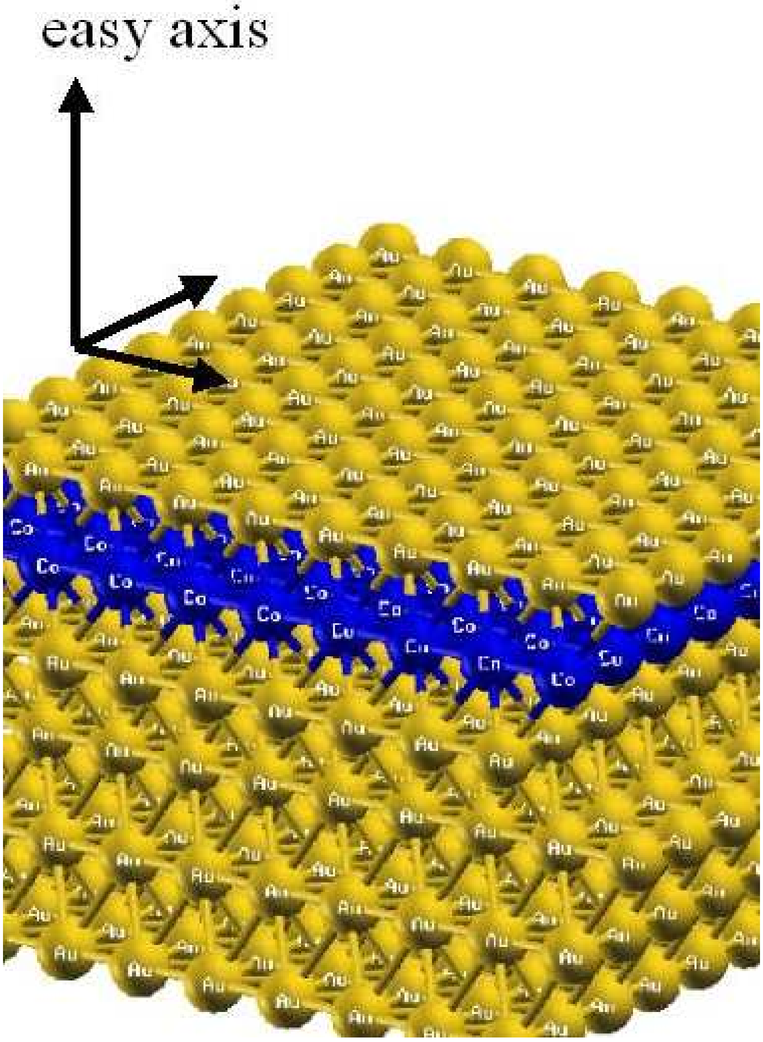

Figure 3.1: Co monolayer on a Au(111) surface with an Au-overlayer.

calculations performed on the unrelaxed structure in LDA approximation by KKR method predict a MAE of 1.4 meV [79].

For the unrelaxed structure the distance between the atoms is the one calculated in the Au-*fcc* bulk: 2.86 Å for LDA and 2.94 Å for GGA. We have gone beyond these calculations by taking into account also the effect of the atomic relaxation on the MAE. After the atomic relaxation the distance between the Au atoms remains the same, while the Co-Au distance decreases to 2.60 Å (LDA) and 2.68 Å (GGA). Table 3.2 shows that, also

Table 3.2: Au(111) supported Co monolayer: MAE and Co spin magnetic moment before and after relaxation. The values reported in Ref. [79] and [82] are also included

	Exp [82]	LDA Ref. [79]	LDA		GGA	
		unrelaxed	unrelaxed	relaxed	unrelaxed	relaxed
MAE [meV]	0.6	1.4	1.95	1.89	3.45	4.00
μ [μ_B]	2.03		1.96	1.82	2.05	2.00

by considering the atomic relaxation, or performing calculations with a different functional (PBE), the theoretical values are sensitively larger than the experimental ones. This overestimation can be possibly explained by taking into account the intermixing at the Au/Co interfaces and/or by surface roughness effects. This argument is supported by previous first principles calculations [83] carried out for Fe$_n$Cu(001) multilayers, where it is shown that the MAE decreases when the symmetry of the surface is reduced.
The experimental Co magnetic moment is 2.03 μ_B. We predict a value of 1.96 μ_B in LDA, and 2.05 μ_B in GGA for the unrelaxed structure. Atomic relaxation reduces the Co spin magnetic moment in both LDA and GGA calculations, by 7% and 3 % respectively. The MAE is instead almost unchanged in the LDA, while it increases with the relaxation from 3.45 meV to 4.00 meV in the GGA case. The MAE values obtained with the GGA functional (Table 3.2) highlights once again that, compared to LDA results, the magnetization aligned perpendicularly to the monolayer plane is favored by this functional, exactly like for the case of the unsupported Co monolayer. Our value of the Co spin magnetic moment obtained with the GGA calculation (2.00 μ_B) is very close to the experimental one (2.03 μ_B) [82]. Both the LDA and GGA theoretical calculations for the relaxed structures predict Co spin magnetic moments that are 3% lower than those of the unrelaxed structures.

In order to better analyze the role of the spin-orbit in the substrate and its influence on the magnetic properties of monolayer, the fully relativistic pseudopotential method offers the possibility to perform calculations in which some atoms are treated including relativistic effects, while others are treated in the non relativistic limit. Since in this case the magnetization is concentrated mainly on the Co atoms it is worth to verify if the computed MAE changes when the Au atoms are described by a scalar relativistic pseudopotential. It turns out that the relativistic description of the Au atoms is essential to predict the correct magnetic properties of this system, since the non relativistic description of the Au atoms modifies the direction of the easy axis by 90°. The easy axis lays parallel to the surface as in the unsupported Co monolayer, and the MAE decreases to 0.80 meV. This indicates that the MAE is not simply given by a change of the Co electron states induced by the potential generated by the supporting Au surface. Au atoms play a more complex and important role in the determination of the MAE. This is a subtle effect since the magnetization induced on the Au atoms by the Co monolayer, is almost zero: the Au atoms closest to the Co monolayer have a magnetic moment smaller than 0.03 μ_B. This behavior deserves a deeper analysis and systems like, for example, a Co monolayer supported by other metal or by insulating surfaces should be considered.

Computational details

The results are obtained with energy cutoffs, for the wavefunctions and for the charge-density, of 30 Ry and 300 Ry respectively, with 52 k points (Monkhorst-Pack mesh (22,22,1)) for the integrations, and with a Methfessel-Paxton smearing of 0.02 Ry. The vacuum distance between the periodic images is of 20 a.u. along the direction perpendicular to the plane. All these parameters deliver convergency in the Co spin magnetic moment and the MAE below 0.05 μ_B and 0.02 meV respectively. The dependence of these quantities on the k-point sampling is displayed in Fig. 3.2, where the vertical line denotes the number of k points used in the calculations. All the other convergency parameters have been tested in a similar way.

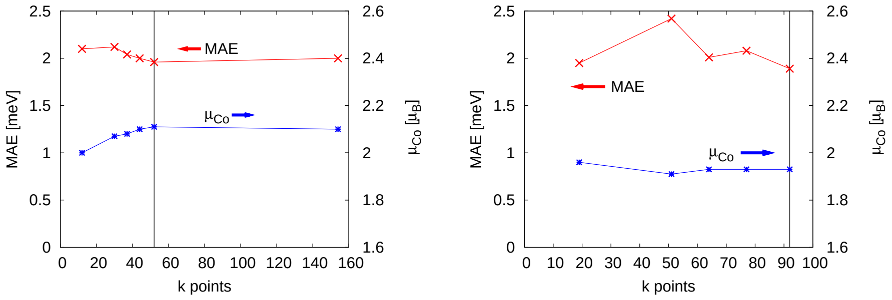

Figure 3.2: Convergency of the MAE and of the Co spin magnetic moment of the unsupported (left) and of the Au surface supported Co monolayer (right) with the number of k points. The following Monkhorst-Pack mesh [67] have been used: 12 k points (9,9,1), 30 k points (16,16,1), 44 k points (20,20,1), 52 k points (22,22,1), 154 k points (40,40,1). The vertical black line indicates the number of k points chosen for our calculations.

3.3 1D: Nanowires

In this section we focus on a 1-dimensional system consisting of a Co nanowire supported by a flat terrace and by a stepped Pt(111) surface, for which the existence of ferromagnetism has been demonstrated [84].

3.3.1 Experimental facts

It is not possible to experimentally realize a 1D structure by aligning Co atoms on a flat surface, since the atoms deposited on the surface would tend to aggregate forming clusters. It has been shown [7], however, that high-density ($5 \times 10^6 cm^{-1}$) arrays of parallel monoatomic chains can be produced by depositing Co below room temperature on a vicinal Pt (997) surface. The STM images in Fig. 3.3 illustrate the regular step structure of the Pt(997) surface and the regular monoatomic Co-wires obtained by decoration of the steps. In the same figure a structural model of the Co-wires over the Pt-surface is reported together with the direction of the easy magnetization axis.

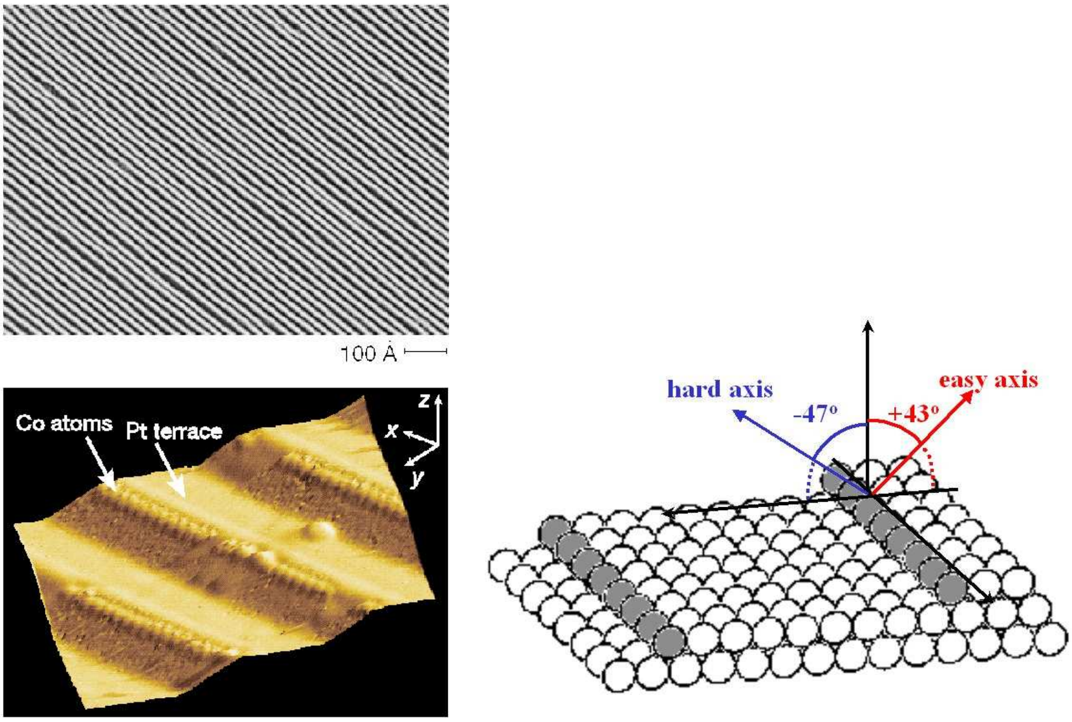

Figure 3.3: STM images taken from [84] of Co nanowires over a (997) Pt-surface (left), and structural model of the Co-wires on this stepped Pt-surface with indication of the easy axis direction.

In the isolated Co atom seven electrons occupy the $3d$ orbitals and because of the Hund's rules the spin magnetization is 3 μ_B. The Hund's rules can be applied to localized atomic orbitals, but the interaction of the Co adatom with its neighbors induces a delocalization of the d electrons, and therefore its spin magnetic moment is expected to decrease both because of the interaction with the substrate and with other Co atoms. This is confirmed by X-ray magnetic circular dichroism (XMCD) measurements [84]. In a wire on the stepped Pt surface, the spin magnetization per atom decreases to 2.08 μ_B, in a Co-monolayer to 2.03 μ_B, and in a Co-hcp bulk to 1.57 μ_B. We note that the spin magnetic moment is larger for lower dimensional structures, where the number of nearest neighbors is smaller and the environment approaches the one of an isolated Co atom. The measured hysteresis loops in the super-paramagnetic and in the ferromagnetic regime for the case of the 1D Co wire

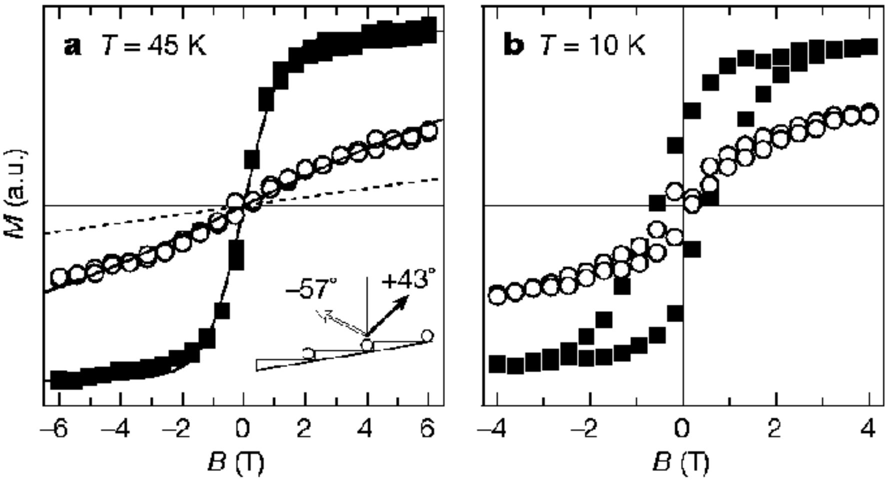

Figure 3.4: Hysteresis loop taken from [84] of Co nanowires over a (997) Pt-surface. In (a) the magnetization is measured in the superparamagnetic regime (over the blocking temperature). In (b) the Co nanowires are below the blocking temperature ($T_B = 15 \pm 5K$).

on the Pt (997) surface are displayed in Fig. 3.4. These measurements show that the easy magnetization axis lays on the plane perpendicular to the wire and its direction forms an angle of 43° with respect to the axis perpendicular to the surface plane pointing toward the "rising versus" of the step. The experimental value of the MAE (2.0 ± 0.2 meV) per Co atom is obtained by fitting the data in Fig. 3.4 (a) with the formula giving the magnetization of the nanowire in the superparamagnetic regime [84]. The inter-chain effects between the wires are found to be negligible.

3.3.2 Theoretical results

Co nanowire on the flat (111) terrace

The relativistic pseudopotential technique was initially used to study the magnetic properties of Co nanowires on a flat Pt(111) surface. This preliminary analysis allowed to separate out the effect of the step from the one of the surface in the magnetic properties of the Co wires. The system was simulated by employing four layers of Pt for the surface, and the Co atoms were located in the positions that the Pt atoms would have in a Pt-*fcc* bulk. Each supercell contains one Co atom and 16 Pt atoms. The distance between the wire and its nearest periodic images on the surface is 8.32 Å. The exchange-correlation energy was calculated using the LDA Perdew-Zunger parametrization. The surface structure was also relaxed according to Hellman-Feynman forces until the total energy per unit cell converged to within 0.15 meV. A scalar relativistic pseudopotential was employed for the geometrical optimization. In both cases the lattice constant is the one theoretically calculated for the Pt-*fcc* bulk (7.414 a.u.). Figure 3.5 shows the nanowire before and after the relaxation: the distance between the Co atoms and the nearest Pt atoms, as well as the Co spin magnetic moment decrease in the relaxation process by 22% and 8% respectively. In the unrelaxed structure the easy magnetization axis is perpendicular to the surface while the relaxation of the atoms rotate the easy magnetization axis by 90°, so that it lays parallel to the wire (see Fig. 3.5). This important effect of the relaxation can be rationalized as follows: in both cases the direction of hard

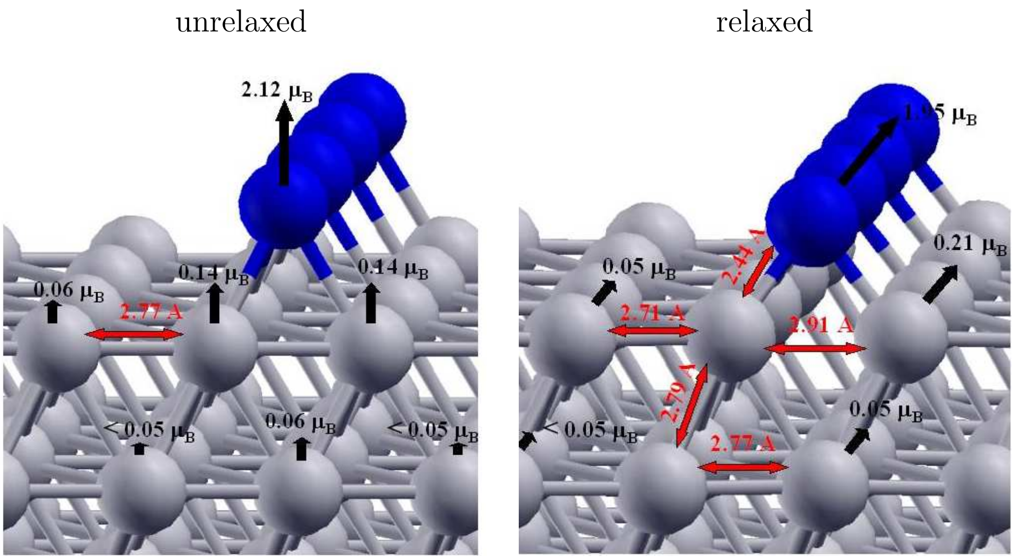

Figure 3.5: Co nanowire on Pt (111) surface with magnetic moments directed along the easy magnetization axis calculated for the unrelaxed (left) and relaxed (right) coordinates.

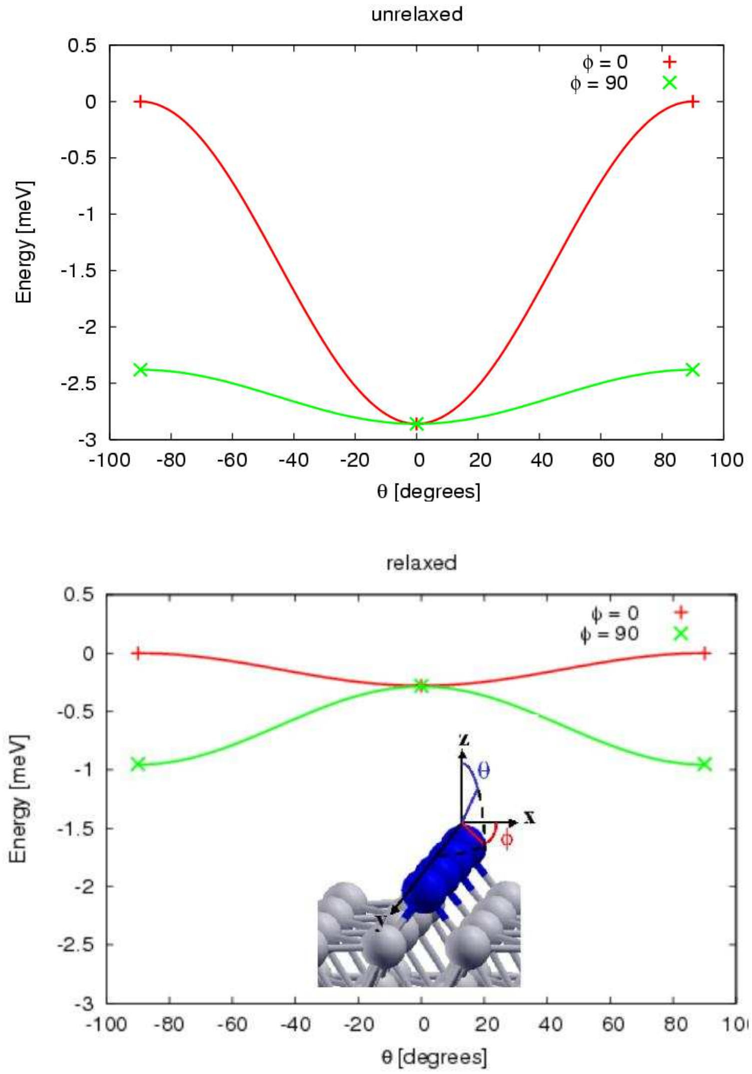

Figure 3.6: Co nanowires on a Pt (111) surface before (top panel) and after (bottom panel) atomic relaxation: total energy as a function of the Co magnetic moment direction (θ and ϕ are defined in the inset).

magnetization is parallel to the surface and perpendicular to the wire. The effect of the structural relaxation on the MAE is to disfavor the magnetization direction perpendicular to the surface and to the wire (see Fig. 3.6); the energy difference between this magnetic configuration and the one with mag-

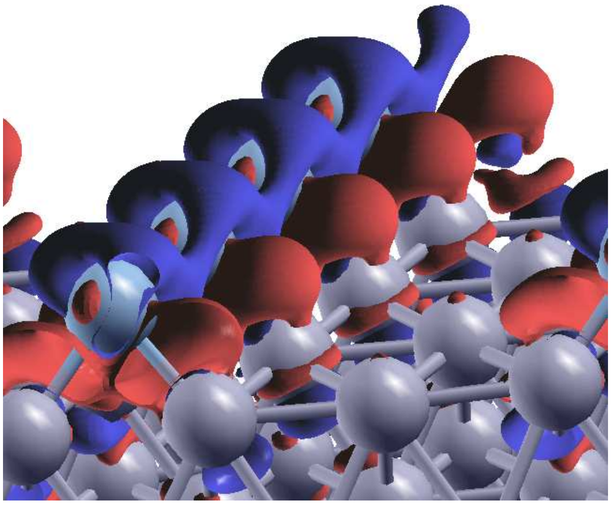

Figure 3.7: Difference between the charge distribution of Co nanowire on the Pt (111)-surface and the one of isolated Co wire + Isolated Pt surface. Blue for positive charge, red for negative charge.

netization parallel to the surface and perpendicular to the wire decreases by 2.6 meV. Concerning the magnetization anisotropy along the surface plane, we notice that in both the relaxed and unrelaxed structures the magnetization direction parallel to the wire is more stable and that the effect of the relaxation is to reduce the gap between the configuration with magnetization perpendicular to the wire and the one with magnetization parallel to it by 1.4 meV. These results are also displayed in Table 3.3 and compared with previous works [85] carried out using the force theorem, embedded-cluster technique and without relaxation of the atomic coordinates. We note that, for the unrelaxed structure, the MAE calculated by the the force theorem is larger than the one predicted by our self-consistent relativistic pseudopotential method.

We observed a charge transfer of 0.21 electrons from the Co-wire to the Pt-surface (Fig. 3.7) both in the relaxed and in the unrelaxed structure. The Löwdin charge analysis reported in Table 3.4 shows that the charge transfer

Table 3.3: Pt(111) supported Co wire. Magnetic moment per Co atom and magnetic anisotropy energy (in meV) expressed as the difference between the total energies taken as a function of θ and ϕ ($E(\theta, \phi)$). θ and ϕ are defined in Fig. 3.6.

	Ref. [85]	unrelaxed	relaxed
$\mu(Co)$ $[\mu_B]$	2.11	2.12	1.95
E(90,90) - E(0,0)	3.3	2.86	0.28
E(90,0) - E(0,0)	1.5	0.48	-0.67

due to the interaction of the Co wire with the Pt surface results from the rearrangement of *s* and *p* orbitals, and, most importantly, it induces a reduction of the polarization resulting from the *d* orbitals, as predicted previously with qualitative argumentations.

Table 3.4: Calculated occupations of the valence orbitals of the Co atom in the Pt(111) surface supported Co nano-wire. In the isolated atom the valence charge is $9 = 4s^2 4p^0 3d^7$. This calculation was performed using a scalar relativistic pseudopotential. In parenthesis the spin polarization calculated as the difference between spin up and down occupations.

	unsupported Co wire	Co wire/Pt(111) unrelaxed	Co wire/Pt(111) relaxed
4S	0.9313 (0.1146)	0.5324 (0.0378)	0.4803 (0.0223)
4P	0.4212 (0.0806)	0.6240 (0.0252)	0.6854 (0.0350)
3D	7.6097 (2.3066)	7.5976 (2.1800)	7.5840 (2.0859)
total charge	8.9622 (2.5018)	8.7539 (2.2429)	8.7497 (2.1433)

Co nanowire on a stepped (111) surface

The geometry of this structure and the coordination of the atoms of the Co wire are completely different form the case of the nanowire on a flat surface. Actually the effect of the step on the nanowire magnetic properties

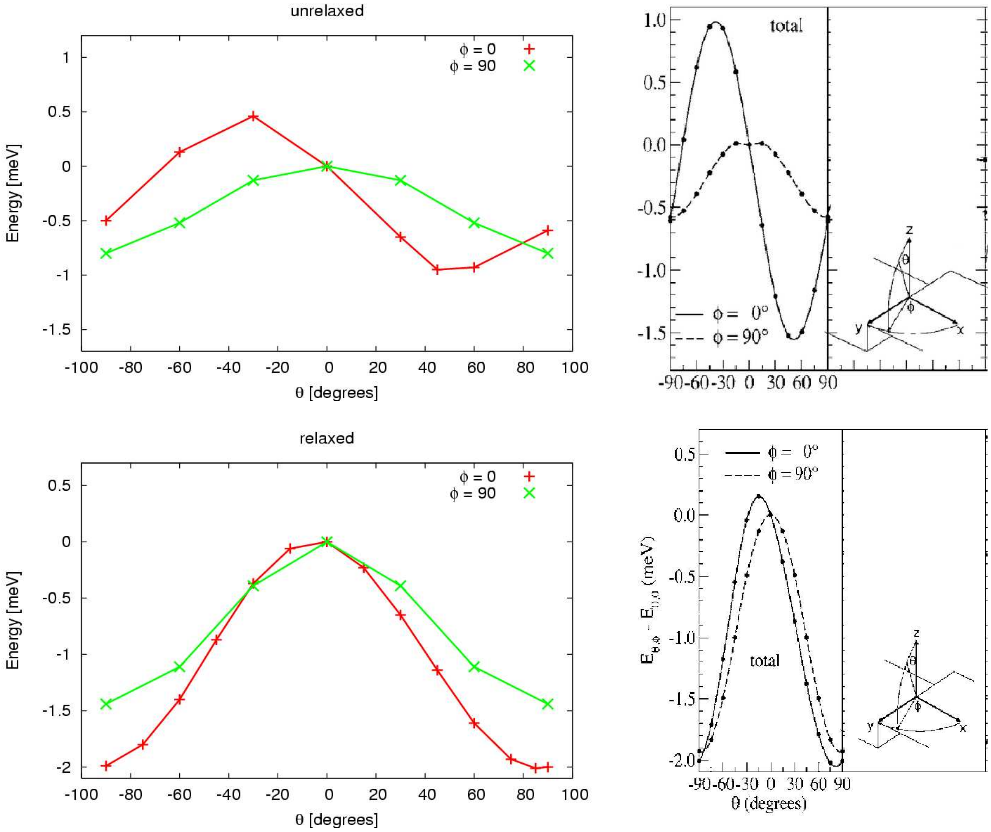

Figure 3.8: On the left panels, total energy of the Co nanowires on a Pt (331) surface before and after relaxation plotted as a function of the Co magnetic moment direction (θ and ϕ are defined in the figures on the right). On the right panels, the same graphics obtained for a (664) structure by Blügel *et al.* in reference [74].

is to change the direction of easy magnetization axis by 90°. Experimentally [84] the easy axis is perpendicular to the wire and forms an angle of 43° with the axis perpendicular to the (111) plane. The easy axis predicted by our calculations and by Ref [74] forms an angle of around 45° with the direction orthogonal to the (111) plane and our value of the MAE is of 1.5 meV, quite close to the experimental measurements. The atomic relaxation of the Co wire increases the angle of the easy axis to 85°, worsening the agreement with the experiment, while the MAE increases to 2.0 meV, in better agreement with the experiment than the unrelaxed value. This is indeed unexpected,

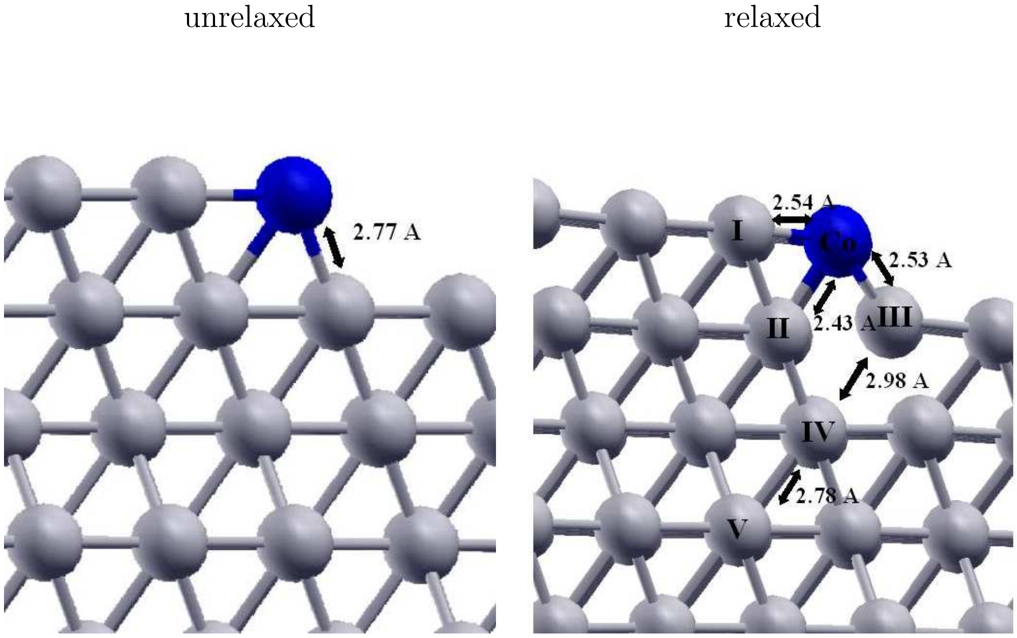
unrelaxed relaxed

Figure 3.9: Co nanowires on a Pt (331) surface before (left) after (right) atomic coordinates relaxation.

but the same result is obtained for a different functional (PBE) and for a different terrace length [74]. All these results are resumed in Fig. 3.8, where the total energy calculated for different directions of the Co magnetic moment is plotted and compared with the results of Ref. [74].

The overall conclusion here is that the direction of the easy axis is extremely sensitive to the relaxation effects and probably neither the LDA nor the PBE functional are accurate enough to predict the relaxed atomic coordinates with the necessary precision. In the unrelaxed structure, the distance between nearest neighbors is 2.77 Å. In the relaxed structure the distances of the Co atoms with the nearest Pt neighbors decrease of 0.2 Å(see Fig. 3.9), while one Pt atom (denoted by III in Fig. 3.9) relaxes outward by 0.2 Å. The spin magnetic moments of the Co atom and of its nearest neighbors are similar to the ones calculated for the nanowire supported by the (111) terrace (compare Figs. 3.10 and 3.5). The energy differences due to the anisotropic effects are in any case very small and stretch the predictive power of state-of-the-art DFT calculations to their limits. Given the importance of

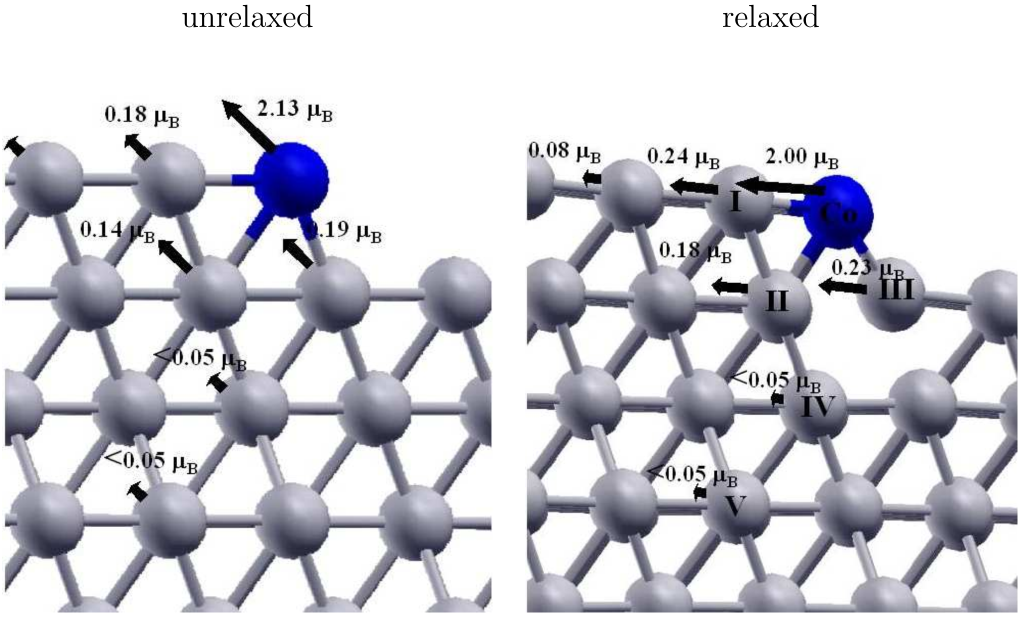

Figure 3.10: Magnetic moments of Co nanowires on a Pt (331) surface before (left) and after (right) atomic coordinates relaxation.

the atomic relaxation in this system, we relaxed the structure with relativistic pseudopotentials starting from the atomic coordinates relaxed with the scalar relativistic pseudopotentials. In chapter 2 it was shown that a perturbative treatment of spin-orbit interaction gives a contribution of second order in the fine structure constant to the total energy. Being defined as the derivatives of the total energy with respect to the ions coordinates, the forces acting on the atoms are also second order in the fine structure constant. Therefore the displacement of the atomic coordinates by relaxation performed by relativistic pseudopotentials is expected to be very small. Indeed the average displacement of the atomic coordinates is of the order of 0.003 a.u. per atom, and we did not observe any change neither in the MAE, nor in the easy axis direction.

A symmetric geometry of the wires in the supercell slab has been considered so that the Co atoms of the wire on the top of the surface and the ones in the symmetric portion of the opposite side of the slab (see Fig. 3.11) have opposite magnetic moment in all the calculations. No differences in the magnetic properties were observed by performing the same calculations with only one Co wire per unit cell (without mirror symmetry along the z axis).The spin magnetization induced on the Pt atoms by the Co wires decreases very rapidly to zero with the distance from the Co atoms as described in Fig. 3.10.

Computational details

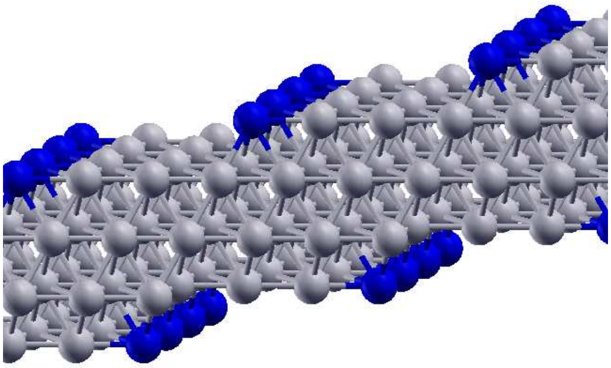

Figure 3.11: Co nanowires on a Pt (331) surface.

The vicinal surfaces are modeled as periodic arrays of step edges separated by terraces. For example, a (x,x,x-2) surface consists of terraces with a width of x full atomic rows and terminated by steps where the step-edge atoms and the surface atoms of the lower terrace form a (111) facet. The calculations were performed for a (331) surface employing the supercell displayed in Fig. 3.11. The cutoffs used for the charge and for the wavefunctions are 30 Ry, and 300 Ry respectively. All the calculations have been performed by using a k-point mesh (5,15,1) and a Methfessel-Paxton smearing of 0.0075 Ry to compute the occupations of the states. These parameters provide an absolute convergency in the total energy of 0.068 meV per supercell.

3.4 0D: Adatoms

3.4.1 Experimental facts

The magnetic properties of a Co adatom deposited over a Pt(111) surface have been experimentally measured [1]. Isolated adatoms can be obtained by depositing minute amounts of Co (less than 0.030 monolayers (ML); $1ML = 1.5\times10^{15} atoms/cm^2$) at temperature T = 5.5 K, low enough to inhibit surface diffusion. The adatom has a spin magnetic moment of 2.1 μ_B. The XMCD measurements performed on this system under the action of a magnetic field show that the easy magnetization axis is directed orthogonally to the Pt-surface with a MAE of 9 ± 1 meV. This system is metastable, and must be maintained at a very low temperature to prevent the clustering of Co. Nevertheless it is also the simplest example of 0D surface supported system. 0D systems are studied also because of their possible implications in magnetic storage devices, and a study on this simple structure could provide useful informations also for technological applications.

3.4.2 Theoretical results

Among the structures studied in this chapter, this is the one with the largest MAE. The fact that it is also the structure with largest Co spin magnetic moment is probably one of the reasons of this high MAE. The spin magnetic moment calculated for the Pt(111) supported Co adatom is 2.18 μ_B for the unrelaxed structure and 2.03 μ_B for the relaxed one. The difference with the experimental value is small in both cases (less than 0.08 μ_B). The relaxation induces a reduction of 8 % of the Co spin magnetic moment and of 17 % of the Co bouds with its nearest neighbors (see Fig. 3.12). Concerning the Co spin magnetic moment, the value predicted by the force theorem [85] for the unrelaxed structure, with the same LDA functional, is in agreement with our results within 0.02 μ_B, as reported in Table 3.5. Similarly to the nanowire case, the Co adatom induces a partial magnetization of the Pt surface. Its nearest Pt neighbors have a spin magnetic moment of 0.20 μ_B. The magnetization then, rapidly decreases so that the other Pt atoms have a spin magnetic moment smaller then 0.06 μ_B.

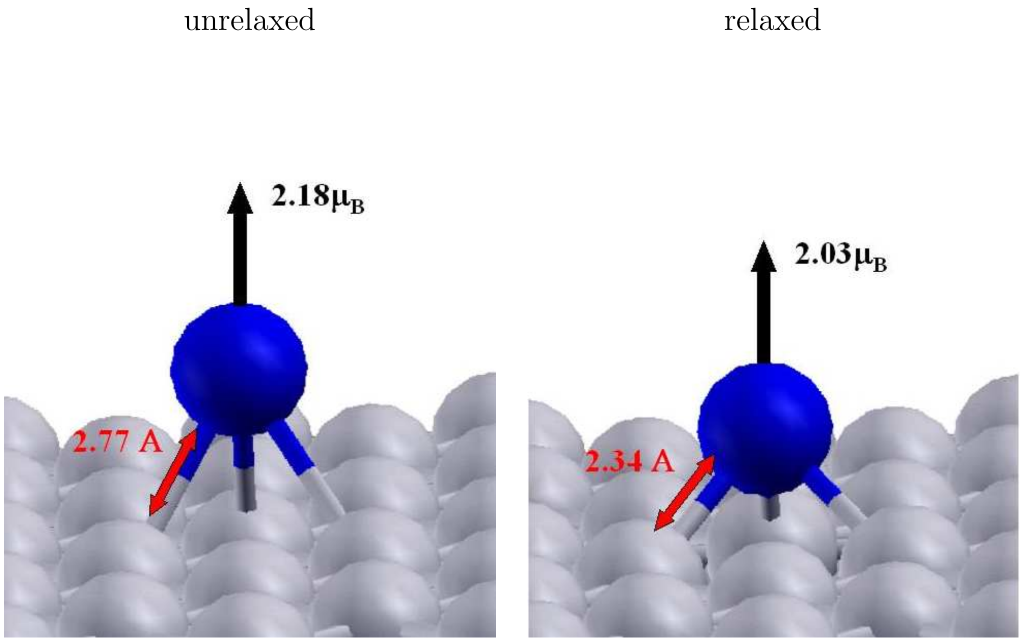

Figure 3.12: Magnetic moments of Co adatom on a Pt (111) surface before (left) and after (right) atomic coordinates relaxation.

Table 3.5: Magnetic moment per Co atom and magnetic anisotropy energy.

		unrelaxed		relaxed
	exp [1]	Ref. [85]	LDA(PZ)	LDA(PZ)
$\mu(Co)$ $[\mu_B]$	2.1	2.21	2.18	2.03
MAE [meV]	9.0	5.9	9.2	4.8

The easy magnetization axis direction is correctly predicted to be perpendicular to the surface both by our calculations and by the calculations performed in Ref. [85] with the force theorem. For the unrelaxed structure we predict a MAE of 9.2 meV very close to the experimental value. We notice that in this system, where the anisotropic effects are sensitively larger than in the previously studied structures, the MAE value obtained by the force theorem is 5.9 meV (3.1 meV less than our value). The atomic relaxation induces a MAE underestimation of 4.2 meV. Similarly to the case of the supported Co wire, this result is unexpected and could depend on several factors, like for example a not enough accurate desciption of the atomic forces because of the exchange-correlation functional used, or the fact that our calculations do not consider the temperature effects.

The occupations of the valence orbitals of the Co atom are displayed in Table 3.6. The total charge is 8.56 electrons (0.44 electrons less than in the isolated atom configuration). Part of the charge is transferred to the Pt surface. The charge distribution on the Co atomic orbitals is similar to the one of the flat Pt (111) surface supported Co wire reported in Table 3.4. Therefore the charge rearrangement of the $4s$ and $3p$ orbitals is mostly a consequence of the interaction with the substrate, and only partially of the interaction between the Co atoms in the nanowire case. Also in this case the most important contribution to the magnetization of the system comes from the the $3d$ orbitals. Compared to the isolated atom configuration, part of the charge of $4s$ and $3p$ orbitals is transferred to $3d$ orbitals, and this induces a decrease of the spin magnetization from 3 μ_B of the free Co atom to 2.1 μ_B of the supported Co adatom.

Table 3.6: Calculated occupations of the valence orbitals of the Co adatom on the Pt(111) surface. In the isolated Co the valence charge is $9 = 4s^2 4p^0 3d^7$. This calculation was performed using a scalar relativistic pseudopotential.

LDA				
	tot charge	4S	4P	3D
	8.5634	0.5040	0.5088	7.5506
spin up	5.4051	0.2690	0.2790	4.8571
spin down	3.1583	0.2350	0.2298	2.6935
polarization	2.2469	0.0340	0.0492	2.1636

The periodic cell has been chosen in such a way that the distance between the adatom and its nearest periodic images is 8.31 Å. The calculations have been performed using a k-point mesh (5,5,1) and a Methfessel-Paxton smearing of 0.0075 Ry. The total energy per unit cell is converged under 0.07 meV.

Conclusions

With the Pt-supported Co adatom we finalize our discussion on Co based low dimensional systems and we can draw some general conclusions regarding all the structures considered in this chapter. For the majority of the systems studied, our results are in agreement with the one obtained by the force theorem, with the only exception of the the Co adatom, where, for the unrelaxed structure we predict a MAE 3.3 meV larger than the one calculated with the force theorem. One possible explanation is that the spin-orbit effects on the charge and magnetization density distribution are more relevant in systems with larger MAE, and therefore play a major role in the determination of the MAE. But there is no evidence of that, and it would be worth to further investigate on the reason of this mismatch.

A general conclusion is that the relaxation of the atoms induces a relevant reduction of the spin magnetic moments. The MAE is also sensitive to the atomic relaxation and in some cases, like the Pt(111) supported Co wire, it can induce an easy magnetization axis rotation of 90°. This extreme sensitivity of the magnetic properties on the atomic positions represents an obstacle for theoretical calculations, since a great accuracy on the determination of the atomic positions is required to correctly calculate the MAE. Furthermore, most of theoretical calculations are performed at zero temperature, and the atomic displacements due to thermal oscillations could affect the MAE value. In some structures the MAE calculated without relaxation are in better agreement with the experimental results. In the case of the adatom, for example, the theoretical value of the MAE calculated for the unrelaxed structure is in perfect agreement with the experiments while the same calculation performed for the relaxed structure gives an under-estimation of the MAE of 4 meV. It would be interesting in future theoretical works to verify if the use of exchange and correlation functionals different from the ones used in this work can improve the description of the relaxation of the atoms and therefore the calculation of the MAE. An other interesting point could be to include the effect of the temperature in the prediction of the relaxed coordinates by phonon calculations or to use directly the coordinates measured experimentally to perform MAE calculations. On the other hand, however, this sensitivity open the way to the possibility to change the easy magnetization axis of a material by sligth modifications of structural geometries, with possible applications in technology.

In all the structures studied, the spin magnetic moments have always been predicted, but no orbital moments have been calculated. The orbital moment is a quantity that can be experimentally measured, and a comparison with theoretical values could give interesting informations also on the anisotropy of a system. The calculation of orbital moments, and their effect on the MAE should be done in future works.

Chapter 4

Molecular nanomagnets

In this chapter I will analyze a class of single molecular magnets, the Tb-Bis-Phthalocyaninato molecules. I will start by studying the unsupported $TbPc_2$ *both in its neutral* $[TbPc_2]^0$ *and charged forms* $[TbPc_2]^-$*. The second part of the chapter deals with the interaction of the neutral molecule with a supporting Cu(111) surface.*

The properties of the magnetic nanostructures studied in chapter 3 are interesting both for scientific and technological aspects. Examples of technological applications of nanomagnets are in quantum computing [4] and information storage media [3], and rely on the capability to address each individual molecular magnet in a two-dimensional array. One of the major scientific and technological challenges is therefore the formation of a highly-regular arrangement of nanomagnets. For this purpose Co adatoms are an example of 0D systems that, even if they have a high MAE, would not form a stable array since they would form clusters degrading the magnetic properties. Therefore the possible applications are limited by kinetic effects. This can be prevented by limiting the Co diffusion over the surface, for example by lowering the temperature. In addition low temperatures are required since the typical blocking temperature of nanomagnets is of few K. with evident technological limitations, that are crucial for applications in which the temperature can not be lowered under a given threshold. A more efficient strategy consists in employing particular nanomagnets consisting of a mag-

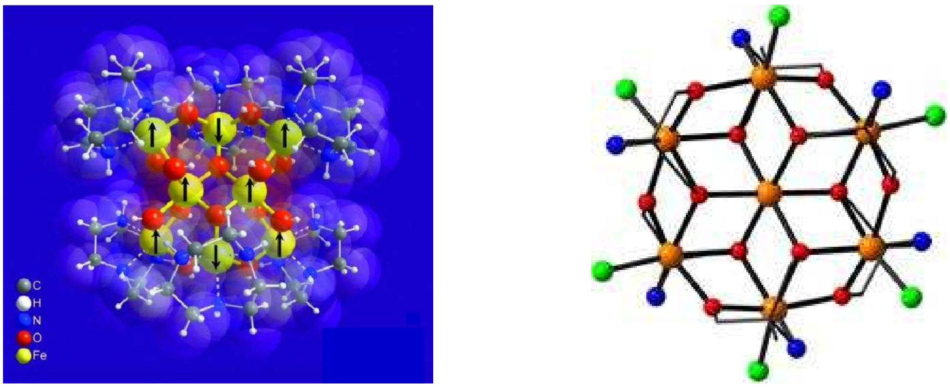

Fe8 complex ($T_B = 2$ K) Mn12 complex ($T_B = 3$ K)

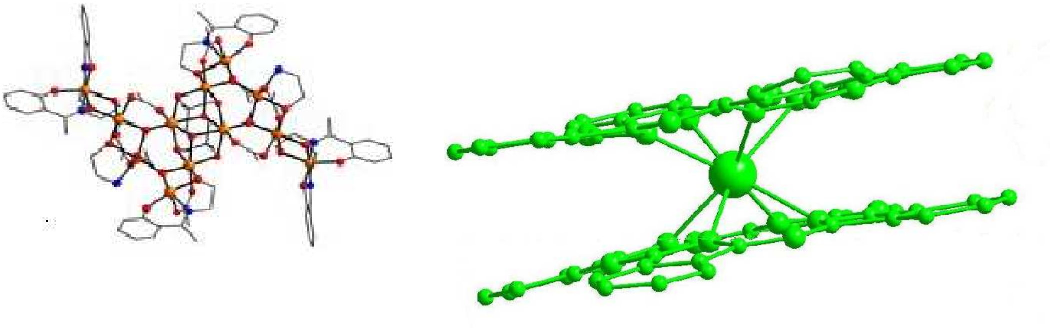

Fe12 complex ($T_B = 3$ K) Tb Double Decker ($T_B = 20$ K)

Figure 4.1: Some popular nanomagnets with their Blocking temperatures reported.

netic center and organic ligands that enable to separate the magnetic centers, thus preventing their clustering, and minimizing their mutual magnetic interaction. Among the molecular nanomagnets, the Bis-Phthalocyaninato molecules based on lanthanides have been identified as the ones with the highest blocking temperature [86], even higher than the one of other popular nanomagnets, like Mn_{12} [9] and Fe_8 [87] complexes having a $T_B \approx$ 3-4 K (see Fig. 4.1). In this class of molecules, the one which presents the highest temperature is the Bis-Phthalocyaninato-Terbium single molecular magnet ($TbPc_2$, also called Tb-double-decker), with a T_B of $\approx$ 20 K [86]. We studied this system in close collaboration with an experimental group at the Max Plank Institut-für Festkörperforshung of Stuttgart, (L. Vitali, and

K. Kern).

4.1 TbPc$_2$: a single magnetization center nanomagnet

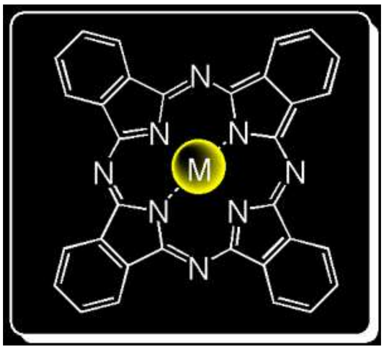

Figure 4.2: Molecular structure of a metal Pc.

Bis-Phthalocyaninato molecules are formed by two coplanar Phthalocyanines (Pc) rotated by 45° with respect to one another and a transition metal or a rare earth ion between them (in this case a Tb atom). In the pure form of phthalocyanines, two of the four nitrogen atoms of the internal ring of the molecule are saturated by two hydrogen atoms. However, in most of the applications, the phthalocyanines are rarely in this pure form, but are bound to other chemical compounds (see fig. 4.2). In many cases these compounds are metal ions which can easily donate to the Pc molecule the two electrons needed to saturate the molecule. The metal ion can be bound to other phthalocyanines forming double or triple deckers and many other kinds of structure. In the case studied in this work two Pc molecules are bound together through a Tb ion forming a double-decker. Overall the ligand system, formed by the pair of Pc molecules, needs therefore four electrons to be saturated. But the Tb atom alone cannot completely saturate the ligand system since this would require the formation of a Tb^{4+} ionic species that is not stable. Only the Tb^{3+} is stable. As a result the TbPc$_2$ molecule is either neutral $[TbPc_2]^0$, and therefore unsaturated, or charged $[TbPc_2]^-$ [88], saturated by an extra-electron.

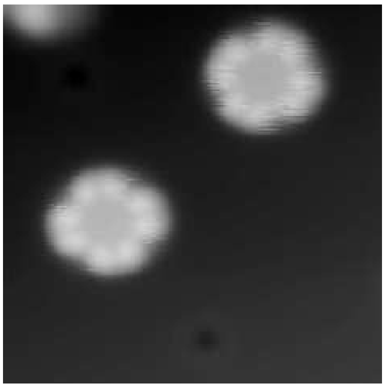

Figure 4.3: STM images provided by Lucia Vitali of Max-Planck-Institut für Festkörperforshung (Stuttgart, Germany). The images were taken in a completely isolated chamber at 10 K (below the double-deckers blocking temperature).

The experimental study has been performed by depositing $[TbPc_2]^0$ molecules on a metallic Cu (111) surface. This operation can not be accomplished by the traditional evaporation techniques, since the structure of the molecule would be damaged during this process. The deposition has been therefore carried out by an innovative technique called nanoimprinting. The most recent STM image in Fig. 4.3 taken at 10 K demonstrates that the plane of the molecules lays parallel to a Cu (111) surface. This was not clear when the present calculations were performed and a vertical absorption geometry was suggested, but it would be important to understand whether the supporting metallic surface modifies the properties of the molecular magnet. We performed a first analysis where we studied properties of the isolated molecule. In a second step we considered the interaction of the $TbPc_2$ molecule with the Cu (111) surface.

I anticipate that the magnetic properties of $TbPc_2$ are not always determined by the metallic center only. In the $[TbPc_2]^-$ the ligand system is completely saturated and does not contribute to the magnetization of the molecule, while in the neutral double-decker the ligand system forms a second spin system whose magnetization density is delocalized over the two Pc molecules. I will start by describing the properties of the charged and saturated unsupported nanomagnet.

4.1.1 The unsupported $[\mathrm{TbPc}_2]^-$ charged nanomagnet

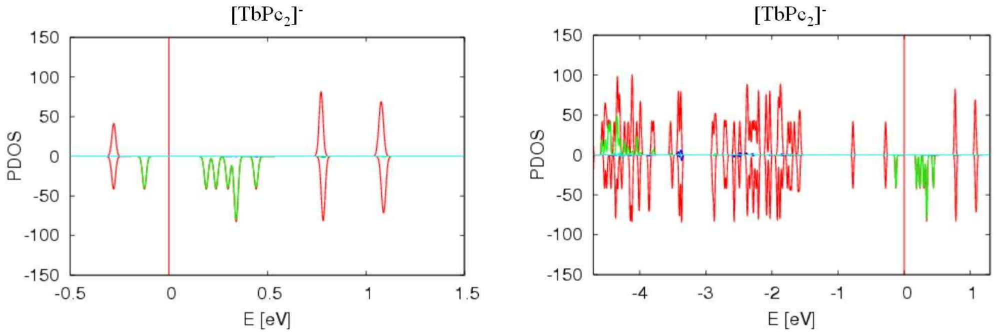

Figure 4.4: Electron energy spectrum of the $[\mathrm{TbPc}_2]^-$ molecule. In green the eigenvalues associated to the Tb atom $4f$ orbitals. In red all the other molecular orbitals.

In the $[\mathrm{TbPc}_2]^-$ nanomagnet, the ligands are saturated and the magnetic properties are controlled by the Tb center. The Tb ion has a formal 3+ ionic charge: with respect to the atomic $6s^2\ 4f^9$ valence electron configuration, three electrons are transferred to the Pc ligands, and the remaining 8 Tb valence electrons are localized on the $4f$ orbitals, which are highly confined near the nucleus. This is clear by analyzing the $[\mathrm{TbPc}_2]^-$ spin resolved density of electronic states (DOS) corresponding to the self-consistent electronic solution displayed in Fig. 4.4. Energies are referred to the Fermi level (black vertical line) located in the middle between the highest occupied and the lowest unoccupied levels. The spectrum shows that the eigenvalues associated to the molecular orbitals of the ligand system form a gap of ≈1 eV around the Fermi energy. The minority Tb $4f$ states, displayed in green in Fig. 4.4, lay in this gap. The Löwdin charge population analysis shows that there are 8.01 and 0.38 electrons in the Tb $4f$ and $6s$ channels, respectively. The ligand system is therefore completely saturated and the metal center is a Tb^{3+} ion. The splitting of 4.5 eV between the spin up and spin down levels is very close to the value of 4.62 eV calculated for an isolated Tb^{3+} ion ([Xe] $4f^8$ electronic configuration) obtained with both pseudopotential and all-electron methods (see Table 4.1). The electronic structure of the Pc-complexated Tb ion is therefore very close to the one of a free Tb^{3+} ion. The magnetic properties of the molecule reside in the Tb^{3+} ion only, characterized by the quantum numbers S=3, L=3, and J=6. As a consequence, the molecule has total spin magnetization 6 μ_B.

Table 4.1: Energy gap between Tb atom $4f_\uparrow$ and $4f_\downarrow$ in different chemical environments. AE = all electron calculation. PS = pseudopotential calculation.

Tb^{+3} environment	ΔE [eV]
Isolated Tb^{+3} (AE)	4.69
Isolated Tb^{+3} (PS)	4.62
Tb ion in $[TbPc_2]^-$	≈ 4.5
Tb ion in $[TbPc_2]^0$	≈ 4.5
Isolated Tb^0 (AE)	3.57

4.1.2 The neutral $[TbPc_2]^0$ molecule

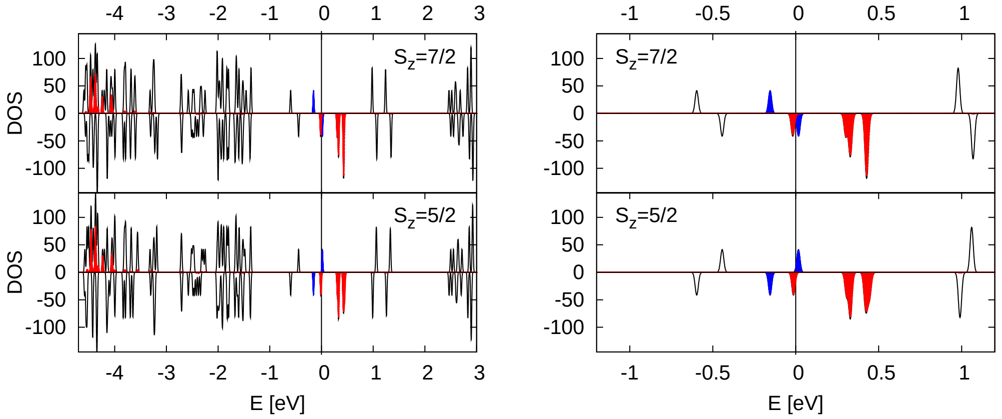

Figure 4.5: Electron energy spectrum of the $[TbPc_2]^0$ molecule (black line). Red solid areas indicate the eigenvalues associated to the Tb atom $4f$ orbitals. Blue solid areas indicate the eigenvalues of the two molecular orbitals responsible for the magnetization of the ligands spin system.

The magnetic properties of the $[TbPc_2]^0$ molecule are determined by two independent spin systems, one strongly localized on the metallic center (Tb ion), the other delocalized over the two Pc ligands. The former is due to the Tb^{3+} $4f$ electrons exactly like in the charged nanomagnet described above, and, in the free-ion limit, would be characterized by the quantum numbers S=3, L=3, and J=6. The latter is due to an unpaired electron (solid blue area in Fig. 4.5) occupying one of the molecular orbitals delocalized over the two Pc ligands and, in the limit of a free unsaturated $[Pc_2]^{3-}$ dimer would be characterized by the quantum number S=1/2. Our calculation predict that these two spin systems are very weakly coupled since two self consistent electronic solutions are identified for the $[TbPc_2]^0$ molecule, differing in the parallel or anti-parallel configuration of the spins localized on the Tb ion and delocalized over the Pc ligands. The energy difference between the two solutions is below 10^{-5} eV. [1] The calculated magnetizations of the $[TbPc_2]^0$ molecule in the two ground states are $\mu_s = 7\mu_B$ and $\mu_s = 5\mu_B$, with the corresponding S_z being 7/2 and 5/2. The difference between the two configurations is given by the polarization of the unpaired electron delocalized over the Pc_2 dimer, as shown by the DOS of Fig. 4.5. Consequently, the the ligand spin up states for the $S_z = 7/2$ solution become spin down in the $S_z = 5/2$ solution, with the same one particle energies. On the contrary, energy and polarization of the Tb-$4f$ states (red areas in Fig. 4.5) in the two electronic states is the same. As a result, molecular spin magnetization differs only in the ligands region but not near the Tb center, as can be seen in Fig. 4.6 where the spin polarized charge density distribution is displayed.

In some cases, only the anti-parallel configuration of the two spin-systems has been observed [89]. This fact could indicate the presence of an antiferromagnetic interaction between them, while our calculations predict that the two spin-systems do not interact magnetically with each other. More recent experiments however carried out on other rare-earth double-decker systems

---

[1] The present DFT calculations describe collinear magnetism and, between the 2S+1 degenerate states allowed for a given S, have access only to the solutions which can be represented by a singular Slater determinant. The accessible solutions have well defined values of S_z and of spin magnetization μ_s, but only the state with maximum S_z is a pure S state, the others being affected by spin contamination. Therefore we will identify the different molecular spin states by S_z and μ_s.

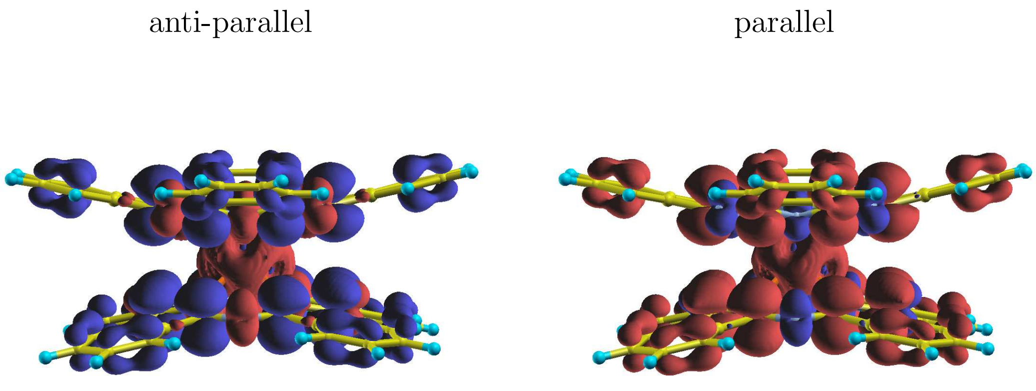

Figure 4.6: $[\mathrm{TbPc}_2]^0$: Spin polarized charge density distribution (red for spin up and blue for spin down) reported for anti-parallel (left) and for parallel configurations.

[90] indicate that the magnetic interaction between the two spin-systems depends on the chemical environment of the molecule [90]. Actually when the distance between the TbPc_2 molecules is larger than 20 Å [90], the two spin-systems are independent the one from the other, in agreement with our calculations.

The charge of the LUMO state, responsible for the magnetization of the ligand system, is delocalized on both the ligands (see Fig. 4.7). This is in agreement with the most recent experimental observations [90]. We however remark that it was previously proposed that the charge would be distributed over only one of the two Pc ligands [89]. For this reason we deliberately broke the symmetry of the molecule along the axis perpendicular to the Tb-DD by applying a step-line external potential (see Fig. 4.8), which would destabilize the symmetric solution therefore allowing the unpaired electron to localize on one ligand only. Starting from this asymmetric electron solution and setting the potential to zero, the symmetric ground state described above was recovered. This reinforces our conclusion that the charge-density corresponding to the LUMO is distributed on both the ligands.

The charge distribution associated with the $4f$ Tb unoccupied orbitals is instead localized in the center of the molecule while the one of the first

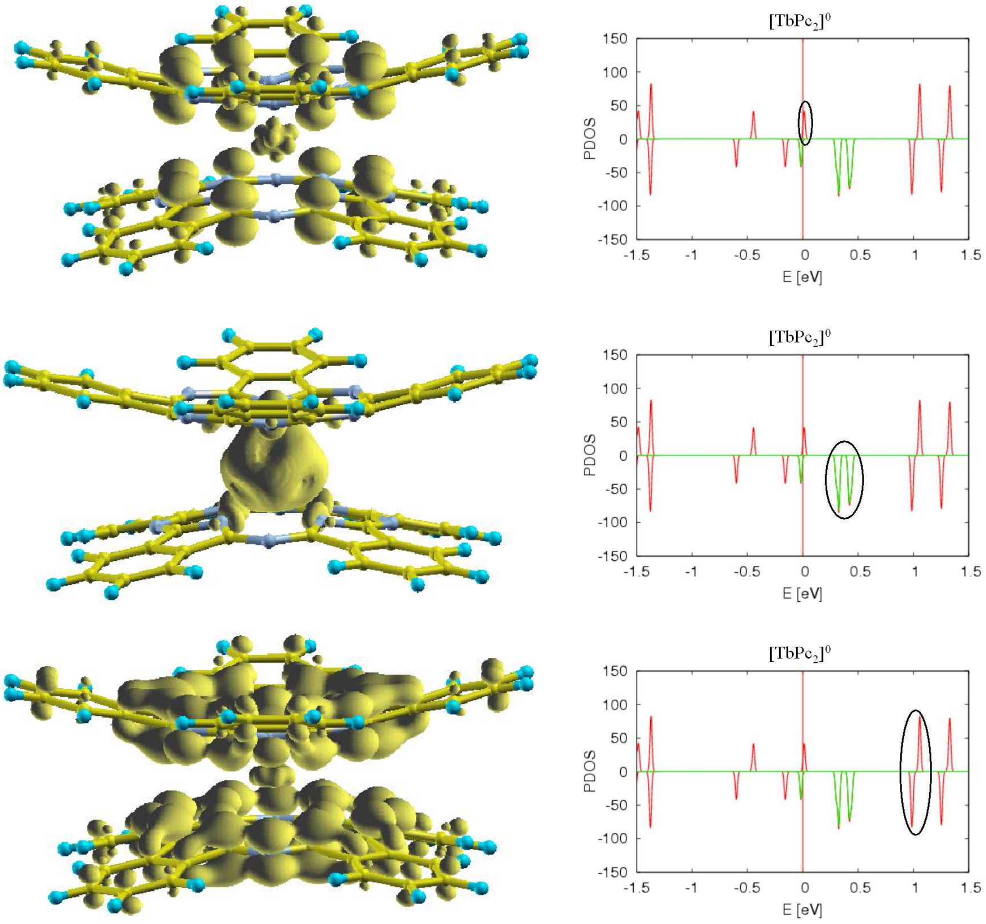

Figure 4.7: Theoretical charge-densities of the LUMO state, the 4f unoccupied states, and the first excited molecular states. The charge density is integrated over the energy scale in the region inside the black circles in the energy spectra on the right.

unoccupied molecular orbital (Fig. 4.7) is delocalized over the Pc ligands, mostly on the Nitrogen and Carbon atoms of the internal part of the phthalocyanines. In Fig. 4.9 a simulated STM image calculated for a bias potential of 1.2 eV is compared with the experimental one taken for a bias of 1.5 eV. The theoretical simulation allows to identify the four pairs of lobs visible in the experimental image as the ones due to the outermost C atoms of the external aromatic rings of the upper ligand.

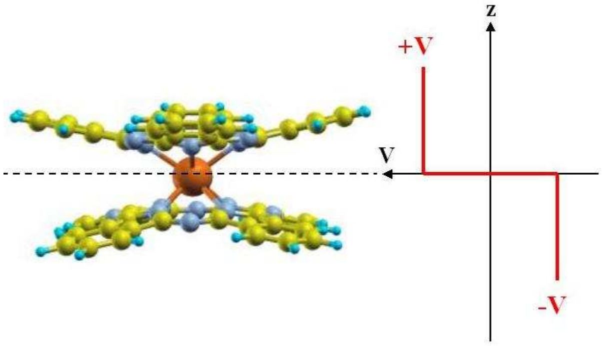

Figure 4.8: External step-potential applied to the Tb-DD molecule.

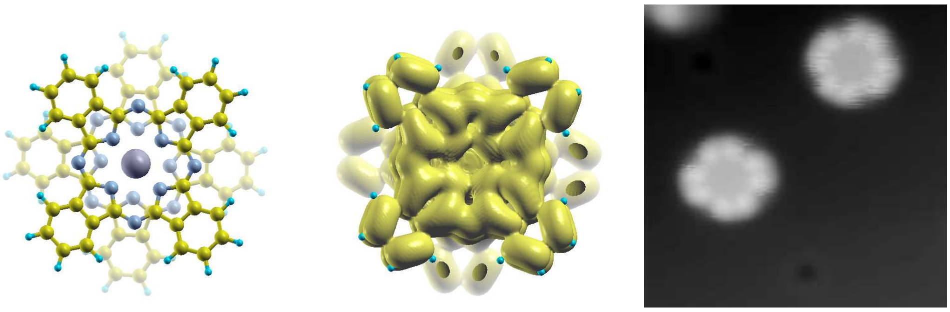

Figure 4.9: Theoretical STM simulated image calculated for a bias potential of 1.2 eV corresponding to the energy of the first excited molecular orbital (center), compared with the experimental STM image with bias potential of 1.5 eV (right).

The magnetic properties were calculated by using scalar relativistic pseudopotentials. The next step would be to estimate the MAE by applying the relativistic pseudopotential method to this nanomagnet. This calculation is complex not only because of the size of the system, but also because of the difficulty in describing lanthanides atoms with pseudopotentials. The work is therefore still in progress.

4.2 $[\mathrm{TbPc}_2]^0$ on the Cu(111) surface

All the calculations displayed above are carried out for an isolated nanomagnet, and the interaction with the supporting surface is not considered.

In this paragraph I will analyze the role of the Cu(111) surface and its possible interaction with the molecule. A charge transfer from the surface to the double-decker could drastically modify the magnetic properties of the nanomagnet and could lead the double decker to the charged variant. Therefore, we first investigated the likelihood for a charge transfer from the metal to the molecule. This can be estimated by comparing the electron affinity of the molecule with the work function of the surface.

The electron affinity of the double-decker was calculated as the difference between the total energies of the neutral and the charged double-decker and resulted to be 3.2 eV. The effect of the electric dipole-dipole interaction between the supercells for the [TbPc$_2$]$^-$ was included by using the Makov-Payne method [91]. The work function was calculated as the difference between the potential energy and the Fermi energy. Both our theoretical value (4.5 eV) and the experimental value (4.94 eV) [92] of the Cu(111) surface are sensitively larger than the calculated TbPc$_2$ electron affinity. Therefore the energy necessary to extract one electron from the surface is not compensated by the energy gained by charging the double-decker. This purely thermodynamic argument let us conclude that the neutral molecule deposited on the surface will not get charged.

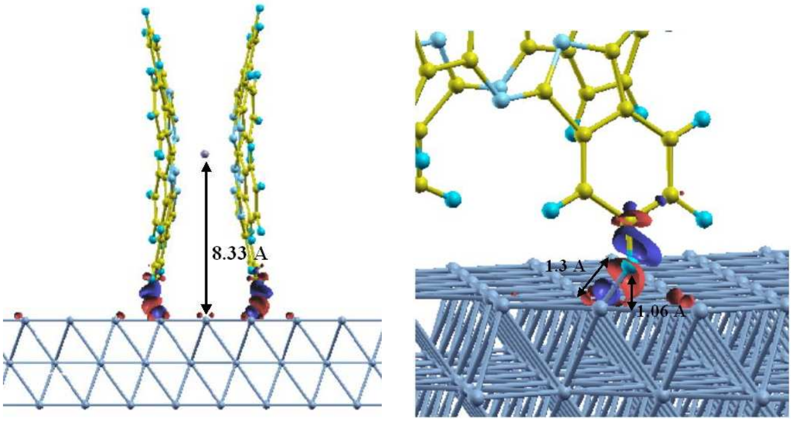

Figure 4.10: Charge transfer from the surface to the molecule. In blue, the electron charge accumulation; in red, the electron charge depletation.

To verify that the electronic properties of the [TbPc$_2$]^0 are not perturbed by the presence of the Cu(111) surface one should perform a calculation with the molecule absorbed on the surface. But this calculation is technically very difficult since the description of the correct electronic structure of the molecule requires a very small value of the smearing parameter (< 0.001 Ry) which is incompatible with a correct description of the metal with a realistic k-point sampling. We have then proceeded with two different approaches representing the extreme cases of a molecule deposited on the metal surface (treating correctly the metal surface, but smearing out the fine details of the electronic structure of the molecule), and the case of a Cu cluster attached to the DD molecule (treating correctly both systems, but being far from the experimentally measured case). Preliminary STM images suggested an absorption geometry in which the double-decker would be oriented orthogonal to the metal surface. The present calculations have therefore be performed according to this initial experimental evidence (see Fig.4.10). The most recent STM data however point to a different absorption geometry in which the molecule is coplanar with the surface. Our previous analysis to evaluate the possibility of a charge transfer from the substrate to the double-decker is based on the calculation of the electron affinity of the molecule, and the work function of the surface, and does not depends on the orientation of the molecule. On the contrary the analysis of the perturbation of the electronic properties of the $[\mathrm{TbPc_2}]^0$ could depend on the orientation of the double-decker, since when the molecule is flat on the surface, the π states can be involved in the molecule-surface interaction. We plan therefore in the future to perform a theoretical simulation also for the case in which the double-decker and the Cu(111) surface are coplanar.

As stated above, our analysis is carried out on a model-system which does not reproduce exactly the experimental conditions. At this stage our goal is to give a qualitative prediction of the charge transfer. In particular we deliberately decrease the distance between the molecule and the surface so that to facilitate any charge transfer. If this procedure does not results in a sizable charge transfer to the molecule, we can safely conclude that the double-decker remains neutral upon absorption of a Co metal surface. To this end, the distance between the molecule and the surface has been reduced to 1.06 Å . I remark that on the basis of other calculations we estimated that

a) $\rho_{DD+Cu(111)}(z), \rho_{DD}(z), \rho_{Cu(111)}(z)$

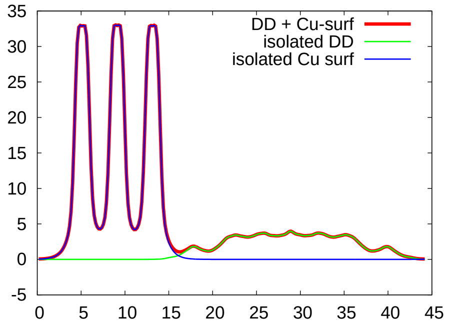

b) $\rho_{DD+Cu(111)}(z) - \rho_{DD}(z) - \rho_{Cu(111)}(z)$

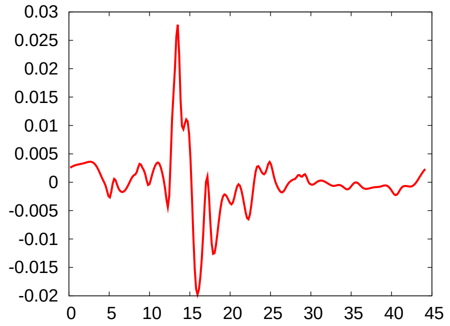

c) $\int_0^z [\rho_{DD+Cu(111)}(t) - \rho_{DD}(t) - \rho_{Cu(111)}(t)]dt$

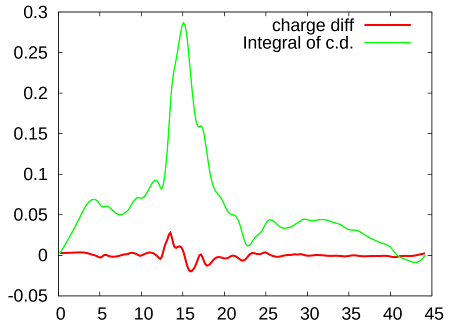

Figure 4.11: Charge densities projected along the z axis. All the quantities are in a.u..

the equilibrium distance between the [TbPc$_2$]^0 and the surface is larger than 2.0 Å.

Even with these conditions favoring the charge transfer, the charge analysis for the first approach shows that charge displacement is very small. The z-projection of the charge densities $\rho_{DD+Cu(111)}(z)$, $\rho_{DD}(z)$, and $\rho_{Cu(111)}(z)$ are displayed in Fig. 4.11 (a). The charge transfer, defined as $\rho_{DD+Cu(111)}(z) - \rho_{DD}(z) - \rho_{Cu(111)}(z)$ and displayed in Fig. 4.11 (b) shows that only the atoms located in an area of ≈ 4 Å around the interface are involved in the charge transfer. The integrated charge difference (Fig. 4.11 (c)), shows that less than 0.3 electrons are transferred from the molecule to the surface. This is further clarified by the 3D plot of the charge difference displayed in Fig. 4.10 (isovalue 0.005).

The charge transfer has also been estimated with the Löwdin charge population analysis. The result is consistent with the previous discussion, since overall 0.4 electrons are transfered from the molecule to the surface, involving only the interfacials C, H, and Cu atoms.

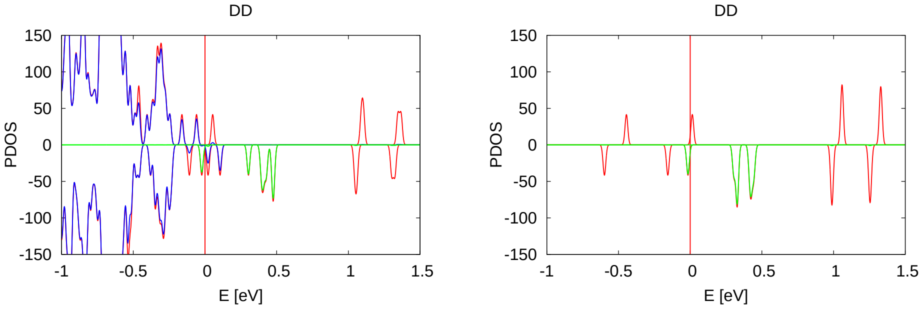

Figure 4.12: DOS of the double-decker in contact with the Cu cluster, and energy spectrum of the isolated double-decker (right).

The same behavior has been observed using the second approach, where the double-decker was put in contact with a cluster of Cu atoms in the same local interfacing geometry described previously. In both calculations, the molecule has a spin magnetization of 6 μ_B. The density of states displayed in figure 4.12 shows that the presence of a metal cluster close to the DD molecule does not modify the electronic structure of the molecule. Also in this case, the calculated charge transfer estimated by Löwdin charge population analysis is of 0.4 electrons. The electronic structure of the isolated DD is not perturbed by the presence of the Cu atoms (see Fig. 4.12). All in all, the electronic structure of the molecule adsorbed on the Cu(111) surface should not be very different from the one of the isolated molecule, and therefore the $TbPc_2$ behaves as a single molecular magnet. This result has to be confirmed by a calculation performed with the molecule in a flat position over the Cu surface.

4.3 Computational details

The DFT calculations were based on the PBE generalized gradient-corrected [19] approximation for the exchange and correlation functional. The ions were represented by ultrasoft pseudopotentials, while the molecular wavefunction and the Fourier representation of charge-density were described with a plane-wave basis set limited by kinetic cutoffs of 40 and 400 Ry, respectively. The calculations were spin polarized.

We used ultrasoft pseudopotentials [14] to simulate the physical properties of the atoms of $TbPc_2$. This was necessary especially to describe the $4f$ Tb atom orbitals with a reasonable number of plane-waves. The isolated Tb atom has a Xenon-core, 2 electrons occupying the $6s$ orbitals and 9 occupying the $4f$ ones. The $6s$ radial charge-density has its maximum at a large distance from the nucleus. On the contrary the charge-density of $4f$ orbitals has its maximum very close to the nucleus (0.56 a.u.). Therefore a norm-conserving description of these orbitals would require a too large amount of plane waves. Actually, as stated above, our calculations (in agreement with the experimental observations) demonstrate that Tb gives to the ligands 3 electrons: 2 from the $6s$ orbitals and one from the $4f$ ones. Given the extreme localization of the $4f$ orbitals, their ionization can perturb sensitively the $5p$ and $5s$ eigenstates. This is why $5p$ and $5s$ channels were treated as semi-cores. The Tb pseudopotential was tested on the TbAu dimer and on the TbF_3 [93, 94] molecular crystal. With respect to the experimental value [95] the calculated TbAu bonding distance is over-estimated by 4%. The TbF_3 molecular crystal is particularly relevant, since the Terbium atom is in a chemical environment very similar to the one present in the $TbPc_2$. It is 8 fold coordinated with 8 fluorine atoms, and has therefore charge +3. Compared to the experimental measurements [96] the lattice constant is overestimated by 2%. The computed spin magnetization is of 24 μ_B per cell, in excellent agreement with the experiments [96].

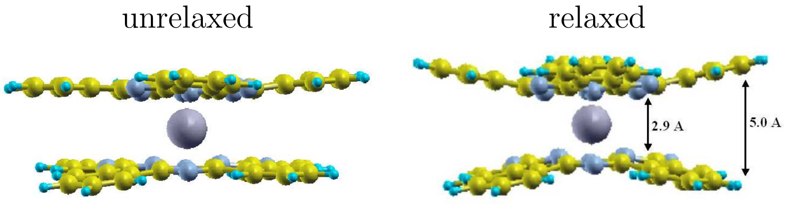

Figure 4.13: Equilibrium structure of the $[\mathrm{TbPc}_2]^0$.

The isolated gas-phase $TbPc_2$ molecule was modeled with a tetragonal supercell with dimensions of 20.10 Å in the Pc molecule plane and of 14.08 Å along the axis perpendicular to the molecular plane. The experimental coordinates obtained from x-ray diffraction of the $TbPc_2$ molecular crystal [97] were fully relaxed according to the Hellmann-Feynman forces until the total energy was converged to less than 0.0003 eV (as shown in Fig. 4.13). The relaxation induces a slight modification of the bonding lengths (within 2%), but it induces a bending of the ligands, so that the external parts of the phthalocyanines tend to increase their mutual distance. This is clear from Fig. 4.13, and from Table 4.2 where the distances projected along the axis perpendicular to the molecule of the outermost C atoms of different ligands is reported, as well as the same distance of the internal N atoms. In the relaxed configuration, the Tb-N bond lengths are between 2.44 Å and 2.46 Å (see Table 4.2), the z-projected distance between the inner N atoms and the outer C atoms belonging to different Pc molecules were 2.88 Å and 5.02 Å , respectively.

The operation was repeated for the charged $\mathrm{TbPc_2}^-$ molecule and the inter-atomic distances are reported in Table 4.2.

Table 4.2: N-Tb distances (Å) for the neutral and charged DD molecule, and projected average distances between the N atoms and the outermost C atoms of different ligands.

	$TbPc_2$	$[TbPc_2]^-$
d N-Tb	2.465	2.490
d N-Tb	2.464	2.494
d N-Tb	2.444	2.477
d N-Tb	2.455	2.501
d N-Tb	2.455	2.486
d N-Tb	2.452	2.494
d N-Tb	2.460	2.483
d N-Tb	2.448	2.495
average N-Tb	2.455	2.490
average d_z N-N	2.875	3.175
average d_z C-C	5.021	4.176

Conclusions

We have implemented a new method to include relativistic effects in the plane-wave ultrasoft pseudopotential scheme [98]. This allows for a combined optimization of the geometric and magnetic structures of complex systems, with an accuracy that had not been possible before. This method has been tested with the calculation of spin-orbit effects on the band structure of some simple noble metals. Spin-orbit effects are responsible for anisotropy energies in magnetic and play a crucial role in the stabilization of magnetism in nano-sized systems.

Our method has been applied to the study of the magnetic properties of Co-based 2D, 1D, and 0D structures (overlayers, wires, and adatoms supported onto a non-magnetic substrate). Our main findings are that magnetic effects, particularly the magnetic anistropy energy (MAE), are larger the smaller the dimensionality of the system, and that they are very sensitive to the local atomic environment of magnetic centers. In the case of a Co nanowire supported on Pt(111), for example, atomic relaxation towards the energy minimum induces a rotation of 90° of the easy magnetization axis. If this sensitivity certainly limits the predictive power of available theoretical and simulation methods, it also opens the way to tayloring the properties of nanomagnets by varying external parameters, such as *e.g.* the temperature, or by engineering the local environment of magnetic centers. The dependence of the magnetic properties on the dimensionality suggests that 0D magnets are ideally suited to enhance the properties of magnetic devices. The formation of highly regular arrangements of single molecular magnets is to date a major scientific and technological challenge. For this purpose magnetic adatoms deposited on a supporting surface would present practical limitations since they tend to form clusters degrading the magnetic properties. This can be prevented by limiting the diffusion of adatoms over the surface, for example by lowering the temperature, with evident technological disadvantages. A promising alternative would consist in employing organic ligands to the magnetic centers apart, thus preventing their clustering. Lanthanide phtalocyanites are ideal candidate molecules for this purpose. In fact we have started a collaboration with the experimental group of K. Kern and L. Vitali at the Max Plank Institut-für Festkörperforshung in Stuttgart to study the properties of terbium phtalocyanite molecules ($TbPc_2$, which consists of a single magnetic Tb center coordinated by two phthalocyanine molecules) deposited on a Cu (111) surface.

The theoretical prediction of the absorption geometry is very difficult in this case because of the size and complexity of the system. As a first step we considered the case of an unsupported $TbPc_2$ molecule in both its charged $[TbPc_2]^-$ and neutral $[TbPc_2]^0$ forms. Following an early suggestion from the experimentalists we then continued our calculations assuming that the molecules are bound perpendicularly to the supporting surface. These calculations showed the interplay between the electronic and the magnetic properties, and indicated that the magnetic properties of this molecule are due to a magnetic moment strongly localized on the Tb^{+3} atom, plus another, very weakly interacting, contribution delocalized over the two ligands. Later experimental evidence seems to suggest that, contrary to what was originally assumed, the molecules lay flat on the metal support. Some preliminary calculations seem to indicate that the magnetic properties of the molecules should be little affected by the interaction with the metal substrate, even in this ‘flat’ adsorption geometry. We have not been able yet to produce a reliable relativistic pseudopotential for Tb. For this reason, the study of spin-orbit effects and of the magnetic anisotropy induced by them will be the subject of future work. Another important methodological advance which will be needed to better characterize the magnetic properties of nanostructured magnetic systems and molecular nanomagnets is the ability to calculate and analyze the orbital contribution to the magnetization. Work along these lines is in progress.

Appendix: Coefficients for relativistic ultrasoft pseudopotentials

This appendix contains the explicit formulation of the U matrix elements and of the Clebsh-Gordan coefficients introduced in the second chapter, and that are necessary for relativistic ultrasoft pseudopotentials scheme.

The U matrix elements can be calculated from the definition of the real form of the spherical harmonics for each $m \neq 0$:

$$Y_{l,|m|}(\Omega)_{cos} = \frac{1}{\sqrt{2}}(Y_{l,|m|}(\Omega) + (-1)^{|m|}(Y_{l,-|m|}(\Omega)), \tag{1}$$

$$Y_{l,|m|}(\Omega)_{sin} = \frac{-i}{\sqrt{2}}(Y_{l,|m|}(\Omega) - (-1)^{|m|}(Y_{l,-|m|}(\Omega)). \tag{2}$$

For $m = 0$, $Y_{l,0}(\Omega)_{cos} = Y_{l,0}$ while $Y_{l,0}(\Omega)_{sin}$ is not defined. Defining for $m \geq 0$, $Y'_{l,m}(\Omega) = Y_{l,|m|}(\Omega)_{cos}$ and, for $m < 0$, $Y'_{l,m}(\Omega) = Y_{l,|m|}(\Omega)_{sin}$, the unitary matrix $U^l_{m,m'}$ reads:

$$\begin{pmatrix}
\frac{-i(-1)^l}{\sqrt{2}}, & \cdots & 0, & 0, & 0, & 0, & 0, & \cdots & \frac{(-1)^l}{\sqrt{2}} \\
\vdots & \ddots & & & & & & & \vdots \\
0 & \cdots & \frac{-i(-1)^2}{\sqrt{2}} & 0 & 0 & 0 & \frac{(-1)^2}{\sqrt{2}} & \cdots & 0 \\
0 & \cdots & 0 & \frac{-i(-1)^1}{\sqrt{2}} & 0 & \frac{(-1)^1}{\sqrt{2}} & 0 & \cdots & 0 \\
0 & \cdots & 0 & 0 & 1 & 0 & 0 & \cdots & 0 \\
0 & \cdots & 0 & \frac{i}{\sqrt{2}} & 0, & \frac{1}{\sqrt{2}} & 0, & \cdots & 0 \\
0 & \cdots & \frac{i}{\sqrt{2}} & 0 & 0 & 0 & \frac{1}{\sqrt{2}} & \cdots & 0 \\
\vdots & & & & & & & \ddots & \vdots \\
\frac{i}{\sqrt{2}} & \cdots & 0 & 0 & 0 & 0 & 0 & \cdots & \frac{1}{\sqrt{2}}
\end{pmatrix}. \tag{3}$$

For $j = l{+}1/2$, where $m = m_j{-}1/2$, we define a σ dependent $(2j{+}1)\times(2l{+}1)$ matrix $U^{\sigma,l,j}_{m_j,m'}$ as follows:

$$\begin{aligned} U^{\uparrow,l,j}_{m_j,m'} &= U^{l}_{m,m'} \\ U^{\downarrow,l,j}_{m_j,m'} &= U^{l}_{m+1,m'} \end{aligned} \tag{4}$$

We take $U^{\uparrow,l,j}_{m_j,m'} = 0$ when $m < -l$, and $U^{\downarrow,l,j}_{m_j,m'} = 0$ when $m + 1 > l$. For $j = l - 1/2$, where $m = m_j + 1/2$, we take

$$\begin{aligned} U^{\uparrow,l,j}_{m_j,m'} &= U^{l}_{m-1,m'} \\ U^{\downarrow,l,j}_{m_j,m'} &= U^{l}_{m,m'} \end{aligned} \tag{5}$$

Moreover, we call the Clebsch-Gordan coefficients $\alpha^{\sigma,l,j}_{m_j}$: for $j = l + 1/2$,

$$\alpha^{\uparrow,l,j}_{m_j} = \left(\frac{l+m+1}{2l+1}\right)^{1/2} \tag{6}$$

and

$$\alpha^{\downarrow,l,j}_{m_j} = \left(\frac{l-m}{2l+1}\right)^{1/2}, \tag{7}$$

where $m = m_j - 1/2$. For $j = l - 1/2$,

$$\alpha^{\uparrow,l,j}_{m_j} = \left(\frac{l-m+1}{2l+1}\right)^{1/2} \tag{8}$$

and

$$\alpha^{\downarrow,l,j}_{m_j} = -\left(\frac{l+m}{2l+1}\right)^{1/2}, \tag{9}$$

Bibliography

[1] P. Gambarella, S. Rusponi, M. Veronese, S. S. Dhesi, C. Grazioli, A. Dallmeyer, I. Cabria, R. Zeller, P. H. Dederichs, K. Kern, et al., Science **300**, 1130 (2003).

[2] P. Wahl *et al.*, Phys. Rev. Lett. **98**, 056601 (2007).

[3] G. Christou, D. Gatteschi, B. Hendrickson, and R. Sessoli, MRS Bulletin **25**, 66 (2000).

[4] N. M. Leuenberger and D. Loss, Nature **410**, 789 (2001).

[5] A. Gelfert and W. Nolting, J. Phys.: Condens. Matter **13**, R505 (2001).

[6] N. D. Mermin and H. Wagner, Phys. Rev. Lett. **17**, 1133 (1966).

[7] P. Gambardella *et al.*, Surf. Sci **449**, 93 (2000).

[8] D. Gatteschi *et al.*, Phys. Rev. Lett. **89**, 257201 (2002).

[9] A. M. Gomes *et al.*, Phys. Rev. B **57**, 5021 (1998).

[10] J. I. Gittleman *et al.*, Phys. Rev. B **9**, 3891 (1974).

[11] J. Korringa, Physica **13**, 392 (1947).

[12] W. Kohn and N. Rostoker, Phys. Rev. **94**, 1111 (1954).

[13] O. K. Andersen, Phys. Rev. B **12**, 3060 (1975).

[14] D. Vanderbilt, Phys. Rev. B **41**, 7892 (1990).

[15] P. Hohenberg and W. Kohn, Phys. Rev. **136**, B864 (1964).

[16] W. Kohn and L. J. Sham, Phys. Rev. **140**, A1133 (1965).

[17] D. M. Ceperly and B. J. Alder, Phys. Rev. Lett. **45**, 566 (1980).

[18] J. P. Perdew and A. Zunger, Phys. Rev. B **23**, 5048 (1981).

[19] J. P. Perdew, K. Burke, and M. Ernzerhof, Phys. Rev. Lett. **77**, 3865 (1996).

[20] R. Martin, Electronic structure basic theory and practical methods, Cambridge, UK Cambridge University Press c2004 **2004** (1971).

[21] D. R. Hamann, M. Schlüter, and C. Chiang, Phys. Rev Lett. **43**, 1494 (1979).

[22] R. M. Dreizler and E. K. U. Gross, "Density Functional Theory", published by Springer-Verlag, Berlin (1990).

[23] U. von Barth and L. Hedin, J. Phys. C **5**, 1629 (1972).

[24] R. Gebauer, PhD. thesis (1999).

[25] J. Kübler, K.-H. Höck, J. Sticth, and A. R. Williams, J. Phys. F: Met. Phys. **18**, 469 (1988).

[26] L. Nördstrom and J. S. Singh, Phys. Rev. Lett. **76**, 4420 (1996).

[27] T. Oda, A. Pasquarello, and R. Car, Phys. Rev. Lett. **80**, 3622 (1998).

[28] D. M. Bylander and L. Kleinman, Phys. Rev. B **58**, 9207 (1998).

[29] R. Gebauer and S. Baroni, Phys. Rev. B **61**, R6454 (2000).

[30] L. M. Sandratskii and P. G. Guletskii, J. Magn. Magn. Mater. **79**, 306 (1989).

[31] V. P. Antropov, M. I. Katsnelson, M. van Schilfgaarde, and B. N. Harmon, Phys. Rev. Lett. **75**, 729 (1996).

[32] V. P. Antropov, M. I. Katsnelson, M. van Schilfgaarde, B. N. Harmon, and D. Kusnezof, Phys. Rev. B **54**, 1019 (1996).

[33] M. Uhl and J. Kübler, Phys. Rev. Lett. **77**, 334 (1996).

[34] Y. Tsunoda, J. Phys. Condens. Matter **1**, 10427 (1988).

[35] O. N. Mryasov, A. I. Liechtenstein, L. M. Sandratskii, and V. A. Gubanov, J. Phys. Condens. Matter **3**, 7683 (1991).

[36] R. Lorenz, S. S. J.Hafner, Jaswal, and D. J. Sellmyer, Phys. Rev. Lett. **74**, 3688 (1995).

[37] M. Liebs *et al.*, Phys. Rev. B **51**, 8664 (1998).

[38] D. Hobbs, G. Kresse, and J. Hafner, Phys. Rev. B **62**, 11556 (2000).

[39] C. Grazioli *et al.*, Phys. Rev. Lett. **95**, 117201 (2005).

[40] M. Castro and D. R. Salahub, Phys. Rev. B **49**, 11842 (1994).

[41] A. M. Rappe, K. M. Rabe, E. Kaxiras, and J. D. Joannopoulos, Phys. Rev. B **41**, 1227 (1990).

[42] L. D. Landau and E. M. Lifshits, Quantum Mechanics (non relativistic theory), Pergamon Press (1976).

[43] U. Fano and W. C. Martin, Z-Dependence of Spin-Orbit Coupling, Topics in Modern Physics (1971).

[44] P. Pyykkö, Chem. Rev. **88**, 563 (1988).

[45] A. H. MacDonald and S. H. Vosko, J. Phys. C **12**, 2977 (1979).

[46] A. K. Rajagopal and J. Callaway, Phys. Rev. B **7**, 1912 (1973).

[47] J. Anton, B. Fricke, and E. Engel, Phys. Rev. B **69**, 012505 (2004).

[48] V. Theileis and H. Bross, Phys. Rev. B **62**, 13338 (2000).

[49] L. Kleinman, Phys. Rev. B **21**, 2630 (1980).

[50] G. B. Bachelet and M. Schlüter, Phys. Rev. B **25**, 2103 (1982).

[51] M. S. Hybertsen and S. G. Louie, Phys. Rev. B **34**, 2920 (1986).

[52] M. P. Surh, M. F. Li, and S. G. Louie, Phys. Rev. B **43**, 4286 (1991).

[53] X. Gonze, J.-P. Michenaud, and J.-P. Vigneron, Phys. Rev. B **41**, 11827 (1990).

[54] K. M. Rabe and J. D. Joannopulos, Phys. Rev. B **32**, 2302 (1985).

[55] L. A. Hemstreet, C. Y. Fong, and J. S. Nelson, Phys. Rev. B **47**, 4238 (1993).

[56] G. Theurich and N. A. Hill, Phys. Rev. B **64**, 073106 (2001).

[57] G. Theurich and N. A. Hill, Phys. Rev. B **66**, 115208 (2002).

[58] R. Caracas and X. Gonze, Phys. Rev. B **69**, 144114 (2004).

[59] A. Dal Corso and S. de Gironcoli, Phys. Rev. B **62**, 273 (2000).

[60] S. C. Watson and E. A. Carter, Phys. Rev. B **58**, R13309 (1998).

[61] R. Gebauer and S. Baroni, Phys. Rev. B **61**, R6459 (2000).

[62] D. Hobbs, G. Kresse, and J. Hafner, Phys. Rev. B **62**, 11556 (2000).

[63] P. E. Blöchl, Phys. Rev. B **50**, 17953 (1994).

[64] M. Methfessel and A. T. Paxton, Phys. Rev. B **40**, 3616 (1989).

[65] G. H. O. Daalderop, P. J. Kelly, and M. F. H. Schuurmans, Phys. Rev. B **41**, 11919 (1990).

[66] S. G. Louie, S. Froyen, and M. L. Cohen, Phys. Rev. B **26**, 1738 (1982).

[67] H. J. Monkhorst and J. D. Pack, Phys. Rev. B **13**, 5188 (1976).

[68] S. Bei der Kellen and A. J. Freeman, Phys. Rev. B **54**, 11187 (1996).

[69] A. Khein, D. J. Singh, and C. J. Umrigar, Phys. Rev. B **51**, 4105 (1995).

[70] R. W. G. Wyckoff, Crystal structures, Vol. 1, published by Wiley, New York (2nd ed.) **1** (1963).

[71] L. Hedin and B. I. Lundqvist, J. Phys. C **4**, 2064 (1971).

[72] S. H. Vosko *et al.*, Can. J. Phys. **58**, 1200 (1980).

[73] M. Weinert, R. E. Watson, and J. W. Davenport, Phys. Rev. B **32**, 2115 (1985).

[74] S. Baud, C. Ramseyer, G. Bihlmayer, and S. Blügel, Phys. Rev B **73**, 104427 (2006).

[75] C. Li, A. J. Freeman, H. J. F. Jansen, and C. L. Fu, Phys. Rev B **42**, 5433 (1990).

[76] S. Baud, C. Ramseyer, G. Bihlmayer, and S. Blügel, Surface Science **600**, 4301 (2006).

[77] B. Újfalussy, B. Lazarovits, L. Szunyogh, G. M. Stocks, and P. Weinberger, Phys. Rev B **70**, 100404 (2004).

[78] G. H. O. Daalderop, P. J. Kelly, and M. F. H. Schuurmans, Phys. Rev. B **50**, 9989 (1994).

[79] B. Újfalussy, L. Szunyogh, P. Bruno, and P. Weinberger, Phys. Rev. Lett. **77**, 1805 (1996).

[80] L. Szunyogh, B. Újfalussy, and P. Weinberger, Phys. Rev. B **51**, 9552 (1995).

[81] B. N. Engel, M. H. Wiedmann, R. A. Van Leeuwen, and C. M. Falco, Phys. Rev. B **48**, 9894 (1996).

[82] P. Beauvillain *et al.*, J. Appl. Phys. **76**, 6078 (1994).

[83] B. Újfalussy, L. Szunyogh, and P. Weinberger, Phys. Rev. B **54**, 9883 (1996).

[84] P. Gambardella, A. Dallmeyer, K. Maiti, M. C. Malagoli, W. Eberhardt, K. Kern, and C. Carbone, Nature **416**, 301 (2002).

[85] B. Lazarovitz, L. Szunygoh, and P. Weinberger, Phys. Rev. B **67**, 24415 (2003).

[86] N. Ishikawa, M. Sugita, T. Ishikawa, S. Koshihara, and Y. Kaizu, J. Am. Chem. Soc. **125**, 8694 (2004).

[87] A.-L. Barra *et al.*, Europhys. Lett. **35**, 133 (1996).

[88] J. Jiang, W. Liu, K.-L. Cheng, K.-W. Poon, and K. P. Dennis, Eur. J. Inorg. Chem. **2001**, 413 (2001).

[89] K. L. Trojan *et al.*, J. Appl. Phys. **69**, 6007 (1991).

[90] G. Gürek *et al.*, Inorg. Chem. **45**, 1667 (2006).

[91] G. Makov and M. C. Payne, Phys. Rev. B **51**, 4014 (1995).

[92] S. L. Hubert *et al.*, Phys. Rev. B **31**, 6815 (1985).

[93] E. Karajamaki, R. Laiho, and T. Levola, Phys. Rev. Lett. **23**, 6307 (1981).

[94] J. Brinkmann, R. Courths, and H. J. Guggenheim, Phys. Rev. B **40**, 1286 (1978).

[95] J. Kordis, K. A. Gingerich, and R. J. Seyse, J. Chem. Phys. **61**, 5114 (1974).

[96] P. E. Hansen *et al.*, Phys. Rev. B **17**, 2866 (1978).

[97] data provided by Mario Ruben of the institute of nanotechnology Research center, Karlsrhue, Germany (private communication) (????).

[98] A. Dal Corso and A. Mosca Conte, Phys. Rev. B **71**, 115106 (2005).

Acknowledgments

I would like to express my gratitude to Stefano Baroni, for giving me the opportunity to work on interesting and amazing subjects, in close collaboration with exceptional people, and for his precious advices and discussions.
My sincere thanks to Stefano Fabris for helping and assisting me with great expertise, for his encouragements and availability. His enthusiasm was invaluable and allowed me to better appreciate my work and to put all my energies in it.
Many thanks to Andrea Dal Corso for supervising my work on the fully relativistic pseudopotentials. Without the implementation of this powerful tool, most of the calculations performed in this thesis would not have been possible.
Many thanks also to Ralph Gebauer, Carlo Cavazzoni and Paolo Giannozzi, whose collaboration was really important especially at the beginning of this work.
I am obliged to all of the people of CM sector with which I had interesting and helpful theoretical discussions.
I would like to thank all of the new friends I met here in SISSA. In particular Guido Fratesi for having borrowed me the illuminating and precious book "Zio Paperone" and Demian Battaglia.
Finally I would like to thank SISSA and Democritos for their financial support.
The period passed here at SISSA was one of the most enjoyable of my life, full of great changes, that I was happy to share with my wife Lidia.
My only regret as president of the SISSA football-team is that we didn't win the Elettra's cup. But I leave a very strong team and I am sure SISSA will win the tournament this year!